ISPRS Journal of Photogrammetry and Remote Sensing 165 (2020) 67–85

Contents lists available at ScienceDirect

ISPRS Journal of Photogrammetry and Remote Sensing

journal homepage: www.elsevier.com/locate/isprsjprs

Long time-series remote sensing analysis of the periodic cycle evolution of the inlets and ebb-tidal delta of Xincun Lagoon, Hainan Island, China

Huaguo Zhang[a,b,c,d,*], Dongling Li[a,b], Juan Wang[a,b], Hongquan Zhou[b,*], Weibing Guan[a,b,c,d], Xiulin Lou[a,b], Wenting Cao[a,b], Aiqin Shi[a,b], Peng Chen[a,b], Kaiguo Fan[a,b], Lin Ren[a,b], Gang Zheng[a,b], Yan Li[a,e]

[a] State Key Laboratory of Satellite Ocean Environment Dynamics, Second Institute of Oceanography, Ministry of Natural Resources, Hangzhou 310012, China
[b] Second Institute of Oceanography, Ministry of Natural Resources, Hangzhou 310012, China
[c] Ocean College, Zhejiang University, Zhoushan 316021, China
[d] College of Oceanography, Hohai University, Nanjing 210098, China
[e] Dongshan Swire Marine Station, Xiamen University, Xiamen 361005, China

ARTICLE INFO

Keywords:
Coastal lagoon
Ebb-tide delta
Shoal sandbar
Tidal channel
Inlet migration
Long time series remote sensing

ABSTRACT

Coastal lagoon–tidal inlet systems occur worldwide, and each has its own unique evolution characteristics in relation to its geographical location, sediment characteristics, and tidal current and ocean wave conditions. However, insufficient observation data means that it is often difficult to fully understand the long-term and short-term evolution of ebb-tidal deltas, and it is even more difficult to monitor and warn against their evolution. This study uses long time-series remote sensing data for the period 1962–2018 to investigate the evolution of an ebb-tidal delta in Xincun Lagoon, Hainan Island, China. Four shoal-sandbar breaching and tidal-inlet migration events were observed, and the corresponding periodic variation characteristics of the ebb-tidal delta were documented. A conceptual model for the periodic evolution of ebb-tidal deltas was also proposed. The results showed that the long-period (15–20 years) evolution was controlled by the effects of seabed friction and tidal-scale lagoon resonance, while the changes in the length of the east sand-spit could be used as a significant early warning indicator for shoal-sandbar breaching and tidal-inlet migration events. In addition, both types of event were jointly triggered by typhoon storm-surges and the accompanying heavy rainfall, strong winds, and strong waves. Thus, the periodic evolution process of the ebb-tidal delta in Xincun Lagoon was determined to be a systematic process that is either controlled or influenced by a series of interconnecting factors. Moreover, we concluded that it is both feasible and valuable to establish a monitoring and early warning framework of ebb-tidal deltas through the use of time-series remote sensing images. The results of this study can improve the existing understanding of the processes and driving factors of periodic shoal-sandbar breaching and tidal-inlet migration, and can also increase safety nourishment for coastal lagoon–tidal inlet systems.

1. Introduction

A typical coastal lagoon–tidal inlet system consists of bays or lagoons, tidal channels, and flood-tidal and ebb-tidal deltas (Hayes, 1980), which occur along sandy or sand and gravel barrier coastlines worldwide (FitzGerald and Miner, 2013). Tidal inlets and their associated ebb-tidal deltas are dynamic features with varying morphology resulting from the complex interactions among waves, tidal flows, and sediment supplies (Hayes, 1980; Pacheco et al., 2011). The morphological modifications may occur over periods spanning from seasons to decades and are characterized by cyclical changes in the position of the inlet channel and by the growth and landward migration of shoals (Garel et al., 2014; Herrling and Winter, 2014; Siegle et al., 2004). However, under the combined action of tidal currents and waves, the sediment load of tidal inlets ultimately results in the adjustment of the tidal inlet morphology and branching migration, as well as the periodic evolution of shoals. As tidal inlets often provide excellent natural navigation channels, and because lagoons offer a safe harbor for the berthing and sheltering of ships, many major ports are situated behind tidal inlets (FitzGerald and Miner, 2013; Ren and Zhang, 1985).

* Corresponding authors at: State Key Laboratory of Satellite Ocean Environment Dynamics, Second Institute of Oceanography, Ministry of Natural Resources, Hangzhou 310012, China (H. Zhang).
E-mail addresses: zhanghg@sio.org.cn (H. Zhang), zhouhq@sio.org.cn (H. Zhou).

https://doi.org/10.1016/j.isprsjprs.2020.05.006
Received 2 February 2020; Received in revised form 21 April 2020; Accepted 8 May 2020
Available online 26 May 2020

Therefore, the stability of tidal inlets has long been an important focus area in the field of coastal engineering and a principal topic in the study of the dynamic geomorphological evolution of estuaries and coasts (Gaudiano and Kana, 2001; Herrling and Winter, 2014; Siegle et al., 2004).

Following the advent of remote sensing technology, related techniques have received continuous attention and have been successfully applied to detect coastal zones, such as coastlines (e.g., Alesheikh et al., 2007; Karsli et al., 2011; Sener et al., 2010; Sridhar et al., 2009; Wang et al., 2013), tidal flats (e.g., Mason et al., 1995, 2010; Ryu et al., 2008; Wang et al., 2019; Zhao et al., 2008), and shallow water topography (e.g., Alpers and Hennings, 1984; Chen et al., 2019; Engenio et al., 2015; Lee et al., 1998; Lyzenga, 1977; Stumpf et al., 2003). The related research literature provides important references regarding the methods and cases for monitoring and analyzing coastal zones. The highly dynamic coastal zone offers a possibility for researchers to attempt to implement long time-series analysis to monitor the evolution of the coast. Since the launch of the Landsat-1 satellite in 1972, numerous satellite images with increasing spatial, temporal, and spectral resolutions have been archived. In addition, with the decryption and opening of images archived by Keyhole satellites (KH), the historical observation period of remote sensing data has been extended back to the 1960s. However, large quantities of satellite images were once isolated in 'information islands' because of the coast and access difficulties (Wang et al., 2019). In the last 10 years, the open data policies of satellite remote sensing in the United States (Woodcock et al., 2008), Europe, and China (Guo et al., 2012) have revolutionized the use of Earth observation data for research and other applications. Benefiting from these open data policies, in recent years, the use of long time-series remote sensing data has allowed for significant progress in the observation and assessment of coastlines (Li and Gong, 2016), salt marsh vegetation (Sun et al., 2008), and coastal aquaculture (Stiller et al., 2019) amongst others. In particular, the analysis of time series data for tidal flats has made important progress at different spatial scales, for example, regional (Murray et al., 2014; Wang et al., 2019), national, continental (Murray et al., 2012; Sagar et al., 2017; Wang et al., 2018), and global scales (Murray et al., 2019). Thus, it can be seen that the merger of multiple satellite images greatly expands the potential for dense time-series analysis, and that remote sensing methods have proven to be valuable for the observation and analysis of the long-term changes that occur in coastal zones.

The southeastern coast of Hainan Island, China, supports a number of coastal sandbar–lagoon–tidal inlet systems, including the medium-sized Xincun Lagoon (Zhang, 1987). The exceptional natural environmental conditions of Xincun Lagoon are conducive to development and utilization; hence, the hydrodynamic conditions (Gong et al., 2008a; Jiang et al., 2009), biological and ecological characteristics (Li and Huang, 2012; Yang and Yang, 2009), sediment characteristics and transport (Gong et al., 2008b; Wang et al., 2016; Yang et al., 2016a), and stability of its tidal inlets have been the focus of much research. In particular, the evolution and stability of tidal inlets in Xincun Lagoon have been studied continuously since the 1980s (Gong et al., 2004, 2006; 2007, 2008b; Yang et al., 2016a; Zhang, 1987; Zhang et al., 1995). Zhang et al. (1995) analyzed the dynamic changes of the ebb-tidal delta in Xincun Lagoon based on historical charts from 1939, 1961, 1975, 1978, and 1981. The authors noted that the east sand-spit (ESS) underwent a westward extension at a rate of 26 m/a during 1939–1961, which was followed by an incident of spit breaching and tidal-inlet migration from 1961–1975. Gong et al. (2004) used five remote sensing images from between 1990 and 2000 to identify another breach of the ESS and tidal-inlet migration for the period 1995–1997. Zhang et al. (1995) and Gong et al. (2004) both pointed out that the main reason for spit breaching and tidal-inlet migration at Xincun Lagoon is that the westward extension of the ESS and tidal channel not only produces an increase in the resistance of the channel, but also decreases the efficiency of the tidal current. These effects subsequently result in a sand-spit break at the edge of the tidal channel under storm or flood conditions. This is similar to the excitation factors of inlet migration and spit breaching, which is one of the methods of tidal branching and sediment migration summarized by FitzGerald and Miner (2013). However, a stability assessment of a tidal inlet cannot explain the large inter-annual variations or the possible longer periodic variations of the tidal inlet systems described by Zhang et al. (1995) and Gong et al. (2004), who used multi-period charts and remote sensing data. The primary reason for this is that the time span and time continuity of observation data used by previous researchers were insufficient, and only minor observations, estimations, or numerical simulation data were used for static evaluations. Therefore, long time-series observation data for tidal inlets are necessary to analyze and evaluate the dynamic changes over a lengthy time period. Accordingly, such an approach would allow the long-term stability characteristics and driving factors of the dynamics of the tidal inlet system at Xincun Lagoon to be distinguished.

The present study therefore attempts to analyze the stability of the tidal inlets and shoal sandbar of the ebb-tidal delta of Xincun Lagoon since 1962 by merging time series of remote sensing images from the KH, Landsat, and HJ-1A/B satellites. Our specific objectives are: (1) to observe the quasi-interannual evolution of the tidal inlets and shoal sandbar between 1962 and 2018 based on long time-series of satellite images, (2) to document and understand the long-term crucial factor and short-term triggering factor of periodic changes to the tidal inlets and shoal sandbar in the ebb-tidal delta, and (3) to propose a monitoring and early warning framework of the evolution of the ebb-tidal delta based on time-series remote sensing images.

2. Study area and data source

2.1. Study area

Xincun Lagoon is located on the southeastern coast of Hainan Island, China, facing the South China Sea (Fig. 1). The lagoon is considered to be of a medium-size (area of ~22 km^2) and is described as a semi-enclosed coastal sandbar–lagoon system with well-developed flood-tide and ebb-tide deltas (Gong et al., 2004; Zhang et al., 1995). The northern side of the inlet throat is an embankment, whereas the southern side consists of the bedrock of Nanwan Hill (Zhang et al., 1995). The tidal current channel is approximately 3–4 km long with a maximum water depth of 8–10 m (Gong et al., 2004), and can be divided into two parts at the throat, which is ~260 m wide. Located between the west coast and the flood-tidal delta, the main flood-tide channel within the lagoon is approximately 1.8 km long with an average depth of ~4 m. These dimensions have been found to be relatively stable over time. The seaward side of the tidal channel that directs the ebb tide is situated between the shoal sandbar that extends westward and the north coast, and has an average water depth of ~3 m, which becomes shallower near the entrance mouth. The length of the exterior region of the channel changes with variations of the shoal sandbar, although its width remains essentially constant (Zhang et al., 1995).

Xincun Lagoon has developed a healthy seagrass community and supports large-scale aquaculture (Yang and Yang, 2009). There are no obvious terrestrial runoff inputs into Xincun Lagoon. The foremost dynamic factors affecting the lagoon are waves and tides, and the water level in the lagoon is mainly controlled by tidal factors. Xincun Lagoon is subject to irregular full-day mixed tides, with contributions from the declination lunar diurnal constituent (O1), the declination lunar-solar diurnal constituent (K1), the principal lunar semi-diurnal constituent (M2), and the principal solar semi-diurnal constituent (S2) (Yang et al., 2016b). Under the combined action of tidal currents and wind-induced currents, the flow field outside the entrance of Xincun Lagoon is characterized by a residual current that turns seawards on the western side of the main tidal channel, and a residual current that turns landwards

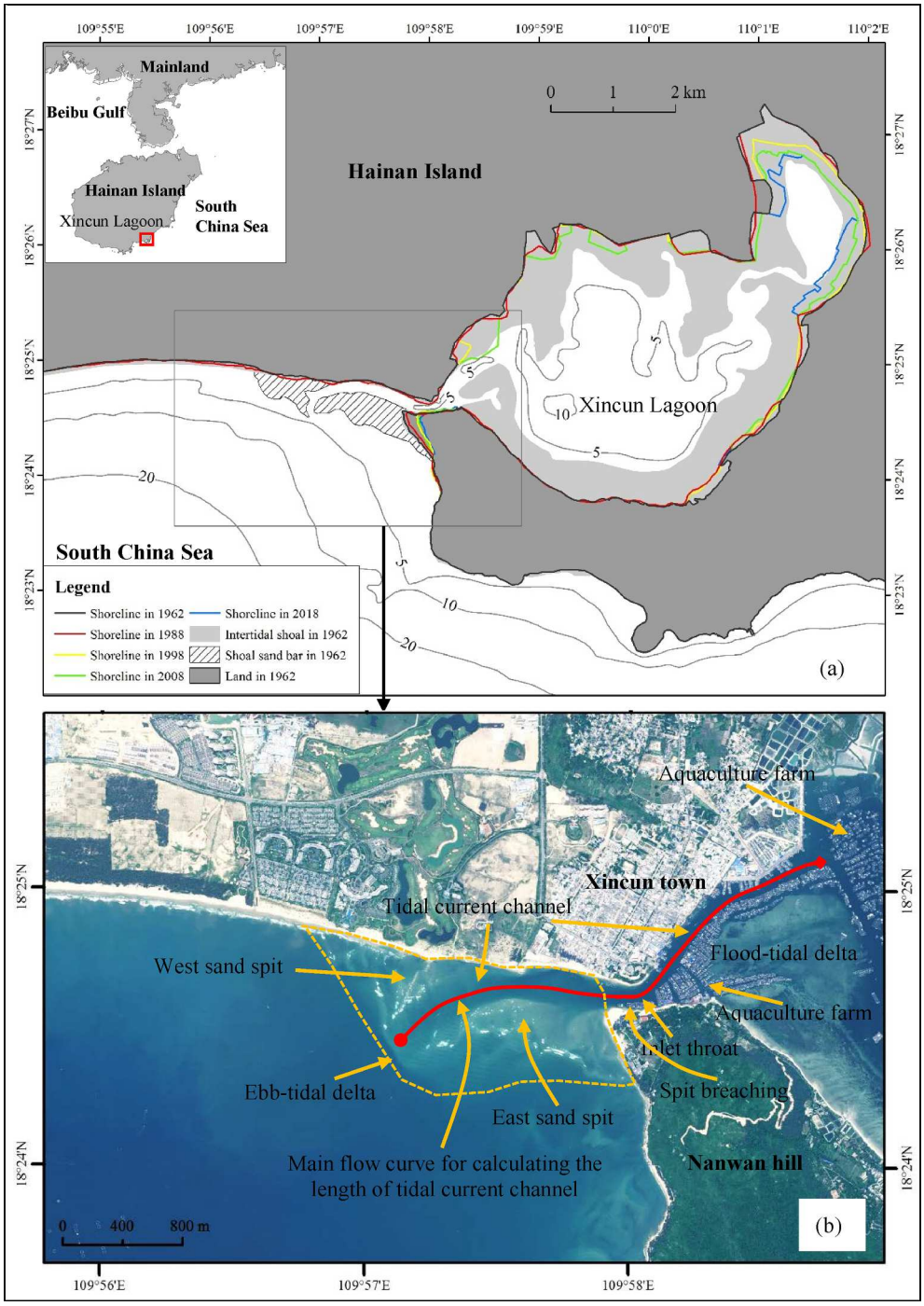

Fig. 1. Study area. (a) Location of Xincun Lagoon and the variation in the shoreline position over time, and (b) WorldView-2 remote sensing image of the tidal inlets of Xincun Lagoon, which was acquired on June 13, 2016. The position of the tidal current channel is indicated by the red line, the dashed yellow line represents the extent of the ebb-tidal delta, and the yellow arrows highlight the lagoon and tidal-inlet features. (For interpretation of the references to colour in this figure legend, the reader is referred to the web version of this article.)

also exists on the eastern side. A clockwise vortex is generated in the southern part of the southern edge of the shoal sandbar. However, under the action of the southward storm waves, it is manifested as east–west coastal currents on both sides of the main tidal channel during the high tide period (Gong et al., 2008).

2.2. Satellite images

We collected 153 scenes of high-quality, cloud-free historical remote sensing data for the study area from acquisition dates ranging from 1962 to 2018. Imaging sensors included KH-4, KH-9, Landsat-1 MSS, Landsat-3 MSS, Landsat-5 TM, Landsat-8 OLI, and HJ-1A/B CCD. The temporal distribution of all remote sensing data is shown in Fig. 2. Within the dataset, there are seven images with a spatial resolution of ~2 m acquired by KH-4 from 1962 to 1968. For the time period of 1973 to 1980, two images with a 6 m resolution from KH-9, two images with a 60 m resolution from Landsat-1, and three images with a 60 m resolution from Landsat-3 were located. There are 79 images from Landsat-5 TM and 57 images from Landsat-8 OLI available at a 30 m resolution since 1986. A gap occurs between Landsat-5 TM and Landsat-

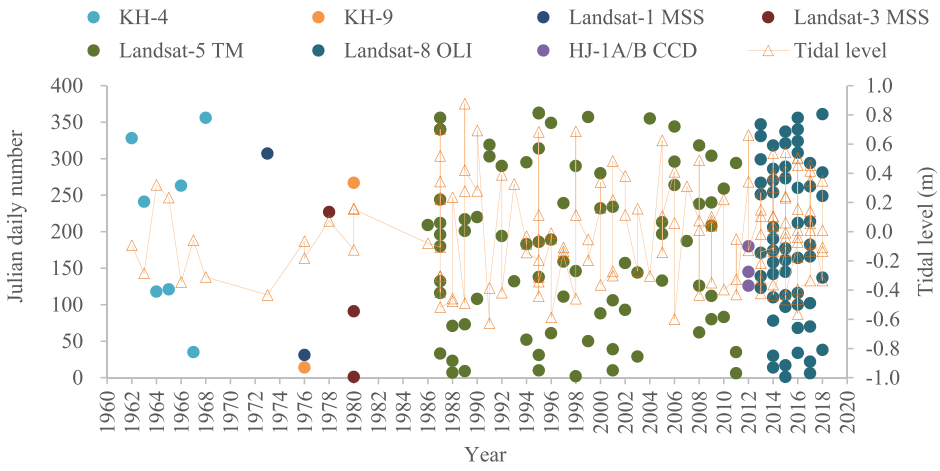

Fig. 2. Sources, imaging dates, and tidal levels for the remote sensing images used in this study.

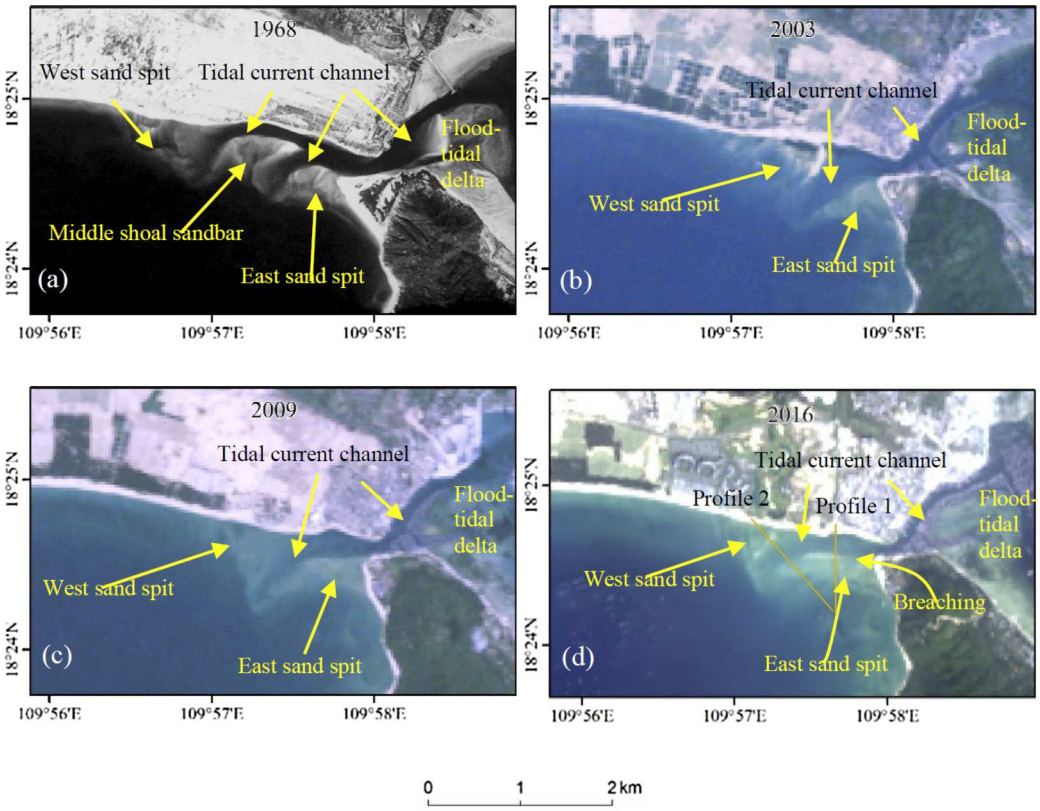

Fig. 3. Remote sensing images in typical years. (a) KH-4 image acquired on December 21, 1968, (b) Landsat-5 TM image acquired on February 1, 2003, (c) Landsat-5 TM image acquired on March 21, 2009, and (d) Landsat-8 OLI image acquired on February 5, 2016, where the two orange lines are the profile locations for water depth and spectral data presented in Fig. 4. (For interpretation of the references to colour in this figure legend, the reader is referred to the web version of this article.)

8 OLI imaging in 2012, which is supplemented by three remote sensing images at an identical spatial resolution from China's HJ-1A/B satellite. In general, there are still two large time gaps in the 56 years from 1962 to 2018, including 4 years from 1969 to 1972 and 5 years from 1981 to 1985. The spatial resolution of the satellite images used in this study therefore varied from 2 m to 60 m, and all of the images were unified to a resolution of 30 m by resampling. In addition, all images were geometrically corrected to the Universal Transverse Mercator North 49th Zone projection system using the WGS-84 datum. Fig. 3 shows the remote sensing images from 1968, 2003, 2009, and 2016, which reveal the different patterns of the shoal sandbars in different years. For example, there was a middle shoal-sandbar (MidSS) in 1968, and the ESS extended westwards significantly between 2003 and 2009 and experienced a breach near its roots in 2016.

As can be seen from Fig. 2, the temporal distribution of the remote sensing data used in this study was not uniform. Fortunately, we mainly focused on the interannual variation of the ebb-tidal delta of Xincun Lagoon. If multiple data were encountered for a given year, the image of the tidal level closest to 0 m was selected for extracting the shoreline and shoal sandbar information; hence, only one image was used for the long-term time series analysis. Of course, in the analysis of the breaching process, all remote sensing data were used for encrypted observations, mainly to determine the beginning and end time of the breach events.

2.3. Additional data sources

A sea chart (No. 16311; 1:25,000 scale) published by China Navigation Publications Press was chosen to obtain the water depths. This chart was published in 2016 and is based on depth data surveyed in 2014. The datum of the bathymetric information is a theoretical depth datum. Based on the image registration of the sea chart and the

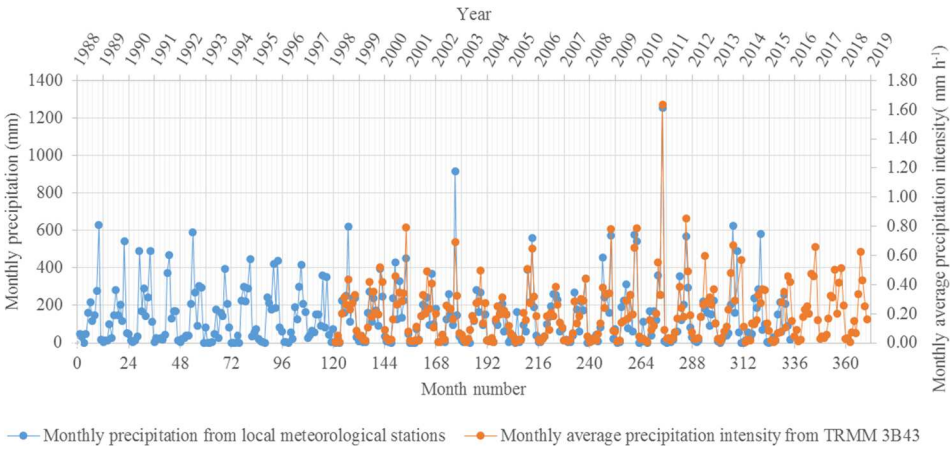

Fig. 4. Precipitation data in the study area from January 1988 to October 2018. The blue dots/line show the monthly precipitation from local meteorological stations, and the orange dots/line show the monthly average precipitation intensity derived from TRMM 3B43. (For interpretation of the references to colour in this figure legend, the reader is referred to the web version of this article.)

Worldview-2 satellite remote sensing image acquired on June 13, 2016, the water-depth points of the chart were derived.

Two precipitation datasets were used in this study (Fig. 4). (1) Monthly precipitation data from local meteorological stations for the period 1988 to 2015 were used to represent total daily and total monthly rainfall (mm). (2) Monthly average precipitation intensity (as hourly data in mm/h) from the monthly precipitation grid data of the Tropical Rainfall Measuring Mission (TRMM) 3B43 (version 7) (downloaded from http://trmm.gsfc.nasa.gov) for the period 1998 to 2018, which cover latitudes 50° S–50° N and longitudes 180° W–180° E at a spatial resolution of 0.25°. These TRMM 3B43 data are compiled in a monthly average global grid dataset composed of TRMM 3B42 data, global point rainfall meter data from the National Oceanic and Atmospheric Administration's (NOAA) Climate Prediction Center Climate Anomaly Monitoring System (CAMS), and global precipitation data from the Global Precipitation Climate Center (GPCC). It was found that these two datasets were well-matched for overlapping time periods, and that most of the heavy precipitation occurred during the autumn, especially in September and October, and occasionally August.

The track and grade data of typhoons since 1949 were collected from the China Meteorological Administration's Tropical Cyclone Data Center (http://tcdata.typhoon.org.cn). By calculating the distance from the typhoon track to Xincun Lagoon, 366 typhoons with a distance of less than 350 km that may have affected Xincun Lagoon were selected for this work. It was found that an average of 5.2 typhoons each year have affected Xincun Lagoon since 1949. According to the monthly distribution of typhoons shown in Fig. 5, 79% of all typhoons were concentrated in the period from July to October. The monthly average precipitation between 1988 and 2015 was highly consistent with the number of typhoons per month, thus indicating that typhoons are the main cause of heavy rainfall in Xincun Lagoon.

The ERA-Interim dataset from the European Centre for Medium-Range Weather Forecasting (ECMWF) provided the reanalysis wind and wave data for the ocean area outside of Xincun Lagoon. These reanalysis data included the wind speed, significant wave height (SWH), and wave direction at 6 h time intervals. An analysis of the dataset was conducted for the period 1979–2018, and the direction of the wind and the waves are uniformly expressed as direction "from". These results are summarized in the wind rose and wave rose presented in Fig. 6. Typically, SWHs were below 1.5 m (~80% of the records), and only during severe storms did the wind-generated SWHs occasionally reach values between 2.5 and 3.0 m. Most wind speeds ranged from 2.0 to 8.0 m/s. The largest and most frequent winds were from the southwest (205°–255°), while ~45% of the wave directions were southwest-west (235°–265°). These data also showed another small peak direction in both wind and waves. Approximately 18% of the wind directions were from between the north-northwest and north (335°–15°), and ~15% of wave directions were from between the north-northwest and north (325°–5°). The wind direction and wave direction of Xincun Lagoon were very well matched, thus indicating that the waves here are basically wind-driven waves, which is consistent with descriptions in the literature (Gong et al., 2008).

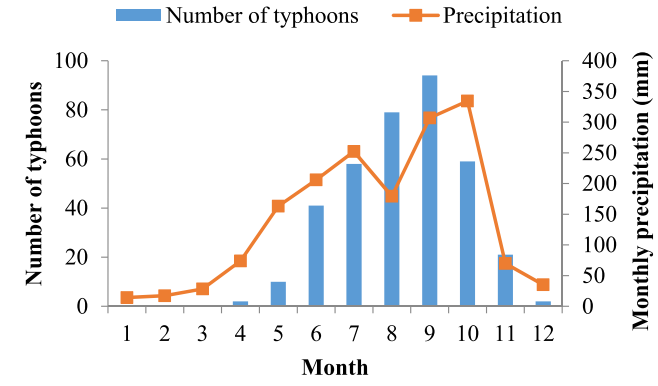

Fig. 5. Monthly distribution of typhoons and precipitation in Xincun Lagoon.

3. Methodology

3.1. Preprocessing

To improve positional accuracy, a Worldview-2 satellite remote sensing image acquired on June 13, 2016 (shown in Fig. 1b), with a high self-positioning accuracy and 0.5 m spatial resolution was used to rectify each scene, with a root mean square error (RMSE) of less than 0.5 pixels for each image.

Then, we used OSU Tidal Prediction Software (OTPS) (developed by Gary D. Egbert and Svetlana Y. Erofeeva from Oregon State University, downloaded from http://volkov.oce.orst.edu/tides/) to calculate the tidal level corresponding to the imaging time of each scene. The tidal level estimation results from the remote sensing images are shown as the orange triangles and solid orange line in Fig. 2. The tidal level datum is the average sea level. Fig. 2 shows that the tidal level balance of most of the remote sensing images was between −0.5 m and 0.5 m. By selecting and processing multi-period remote sensing images for a given year, the tidal level gap in most years could be ensured to be within 1.0 m. Shoreline identification from 30 m resolution remote sensing images was subject to horizontal deviations of less than one pixel due to tidal ranges, which had a limited impact on the long time-series analysis.

3.2. Extraction of shoreline and shoal sandbar

In this study, the shoreline is defined as the demarcation line between the land and water, and the shoal-line is defined as the

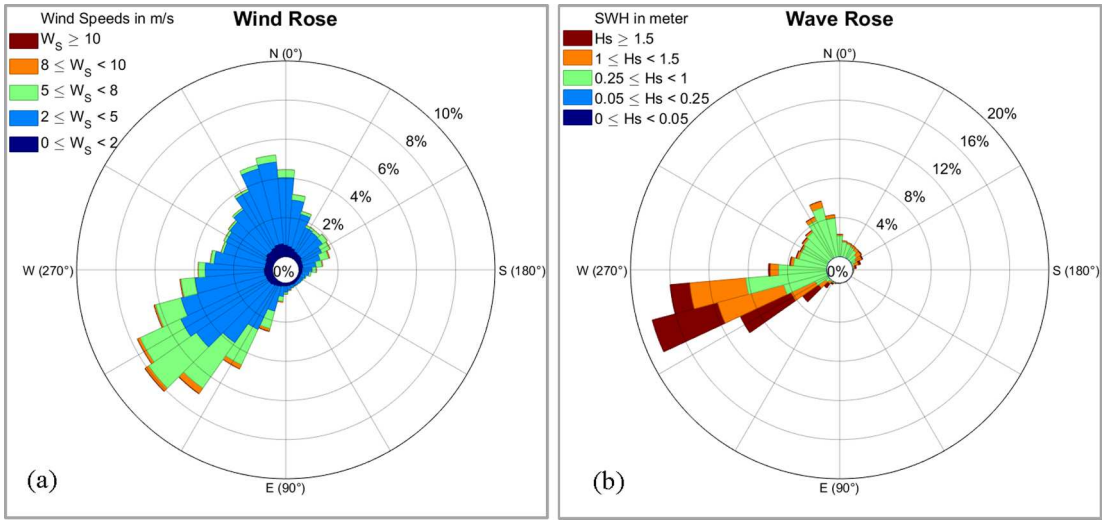

Fig. 6. (a) Wind rose and (b) wave rose based on the ERA-Interim dataset at 109.875° E and 18.375° N for the period 1979 to 2018.

demarcation line between the shoal sandbar and ocean, also named as the boundary of the shoal sandbar. These determinations form the basis for extracting information on lagoons, tidal inlets, and shoal sandbars. The primary remote sensing data used in this study were multispectral data from Landsat-5 TM and Landsat-8 OLI after atmospheric correction. Shoreline information can be obtained in the near infrared band by the significant differences between land and water.

However, shoal-line information is located underwater, and its location needs to be determined by a comprehensive analysis of the water depth and spectral characteristics. For this, we used the logarithmic ratio model proposed by Stumpf et al. (2003) to retrieve the water depth data from WorldView-2 images acquired on June 13, 2016 (shown in Fig. 1b), with a high resolution of 2 m, as based on the depth data from the chart by avoiding the area where the shoal sandbar changed. The inversion depth results are presented in Fig. 7a, whereby the evaluation results (Fig. 7b) yielded an RMSE error of 0.98 m in the 0–8 m depth region and R^2 of 0.8151. These results were deemed acceptable for the inversion of the water depth in the near-shore turbid region, and whose influence was limited for the determination of the shoal-line according to the variation characteristics of water depth in this study.

On the basis of the inversion results, the water depths for the two profiles shown in Fig. 7a were extracted, and the spectral profiles of visible bands including the blue, green, and red bands from the Landsat-8 OLI image (Fig. 3d) acquired on February 5, 2016, were obtained, as shown in Fig. 7c and d. It can be seen that the radiation value of each band decreased as the depth deepened significantly from the land to the land–water boundary, which should represent the location of the shoreline (L1). The transect line continued seawards and passed through about two pixels (equivalent to ca. 60 m) into a nearly unchanged region with a water depth of > 2.0 m. The radiation values of the three bands in this region were as follows: blue band = 64.1 W m^{-2} sr^{-1} μm^{-1}, green band = 48.3 W m^{-2} sr^{-1} μm^{-1}, and red band = 26.2 W m^{-2} sr^{-1} μm^{-1}, which should represent the tidal current channel with a width of ~180 m. At increasing distances from the shoreline, the radiation intensity of the three visible bands increased again, and the depth reduced sharply in relation to the proximity to the shoal sandbar. Thus, the abrupt change of the spectral characteristics also reflected the abrupt change of water depth, and based on this, the shoal sandbar could be located between L2 and L3. Similar to profile 1, profile 2 in Fig. 7d reveals that the shoal sandbar was located between L1 and L2, and L3 and L4, whereby the tidal channel was determined to be between L2 and L3. However, the spectrum and water depth characteristics along profile 2 closer to the estuary of the tidal current channel were found to be different from those of profile 1 in two aspects. One was that there was a shoal sandbar area after leaving the land before entering the tidal current channel. The other was that the spectral differences between the tidal current channel and shoal sandbar were not as significant as those along profile 1, which was probably due to the higher amount of suspended sediment induced by the shallower water depth.

Due to the influence of highly turbid waterbodies and their spatio-temporal differences, the determination of shoal sandbar areas is therefore difficult when relying solely on spectral data. Instead, manual interpretation or correction is highly necessary when using the relative spectral differences between the tidal channel, outside waters, and shoal sandbar area, especially for some KH remote sensing data with only panchromatic bands. After resampling, all of the images had a resolution of 30 m and the interpretation error was one pixel; hence, the horizontal error of the shoreline and shoal sandbar was ~30 m. According to the tidal level analysis (Fig. 2), the tidal level fluctuation in the study area is not particularly large. As shown in Fig. 2, during the period 1962–1980 when there was only one remote sensing image, the tidal level fluctuation range was between −0.4 and 0.4 m. Referring to the two typical water depth profiles in Fig. 7 c and d, the maximum horizontal deviations of the shoreline and shoal sandbar were approximately 30 m and 50 m, respectively, under the maximum 0.8 m tidal range. When these two errors were superimposed, the length error of shoal sandbar was < 80 m. The average length of the shoal sandbar was approximately 1000 m and the average relative error was < 8%. As this study focuses on the long-term change trend of the shoal sandbar and the associated geomorphological issues, it can be considered that these extraction errors will not have a great impact on the analysis of the change trend; hence, we think that they are acceptable.

The shoreline and shoal-line were interpreted according to Fig. 7, whereby the shoal-line was located at a water depth of ~1.0 m. Information regarding the shoreline and shoal-sandbar locations in the time-series remote sensing images since 1962 was extracted by threshold segmentation, appropriate manual correction, and smoothing. Fig. 1a displays the shoreline locations in 1962, 1988, 1998, 2008, and 2018, as well as the shoal sandbar location in 1962.

After extracting the contour information for the shoal sandbar, the corresponding area patches were obtained through topological calculation. Then, the geometric centers of the patches were calculated as the center points of the shoal-sandbar patches (CPSPs), which were used for the analysis of the center trajectory of the shoal sandbar. In addition, the tidal channel was determined using the spatial positions of the shoal sandbar and shoreline. The centerline of the tidal channel along its

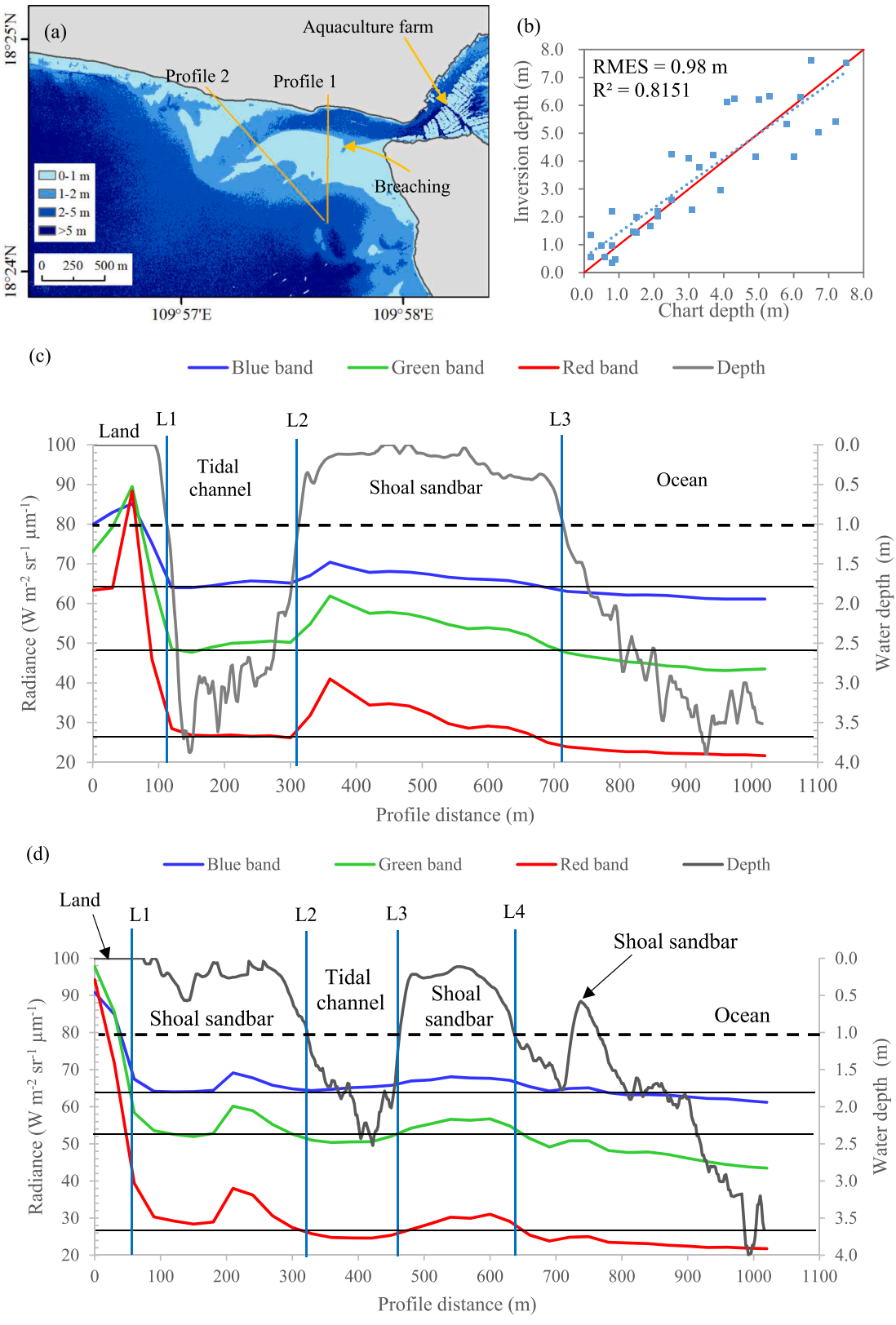

Fig. 7. Diagrams of interpretations of the shoreline and shoal sandbar: (a) inversion water depth from the WorldView-2 image acquired on June 13, 2016 (Fig. 1b), where the two orange lines are the two profile locations for analyses of water depth and spectral characteristics, (b) the accuracy verification of the inversion water depths, and (c) profile 1 and (d) profile 2 of the water depth and spectral characteristics across the tidal channel and shoal sandbar. The horizontal black solid lines represent radiation values for the various bands within the tidal channel, and the horizontal black dashed lines represent a depth of 1.0 m. L1 marks the position of the shoreline, and L2, L3, and L4 represent the boundaries of the shoal sandbar.

direction was calculated as the main courses of the tidal current channels (MCTCs), which was used to analyze the channel centerline swing.

3.3. Helmholtz resonance model

Ocean tide resonance phenomena are pervasive, especially within coastal and offshore settings. The Bay of Fundy in Canada displays the largest half-diurnal tidal component in the world, and is therefore considered to be the classic example of a bay with tidal resonance (Garrett, 1972; Greenberg, 1979). Prandle and Rahman (1980) postulated that tidal resonance causes a sharp increase in the tidal range.

The Helmholtz resonance model is one of the classic theories of tidal resonance. Miles and Lee (1975) studied the theory and method of Helmholtz resonance as applied to harbors. Since then, the Helmholtz resonance model has been used to study actual sea regions at different scales, for example, the Waden Sea (Maas, 1997), Juan de Fuca Strait and Strait of Georgia (Sutherland et al., 2005), Lunenburg Bay in Canada (Mullarney et al., 2008), and Málaga port in Spain (Sammartino et al., 2014). Helmholtz resonance was applied in this research because the studied lagoon system is very similar to the classic Helmholtz resonator as it has a huge near-round container (i.e., Xincun Lagoon) and a thin tube mouth (i.e., the tidal channel).

The Helmholtz resonance frequency and period are calculated without considering the damping effect. Assuming that a bay is connected to the outer sea through a tidal channel, the formula for calculating the Helmholtz resonance angle frequency of the tidal resonance in the bay is given by Eq. (1):

$$\omega_0 = \sqrt{ghW/LS} \tag{1}$$

where g is the gravitational acceleration, S is the lagoon area, and L, W, and h are the length, width, and depth of the tidal channel, respectively. Thus, the Helmholtz resonance period can be calculated by Eq. (2):

$$T = 2\pi/\omega_0 \tag{2}$$

4. Results

4.1. Lagoon

Areal estimates of the characteristics of Xincun Lagoon from 1962 to 2018 were obtained by spatial topological analyses based on the time series analysis and are shown in Fig. 8a. Prior to 1980, the area of the lagoon was 22.85 km^2, after which, the area stabilized at 22.4 km^2 from 1986 to 1997 (red circles in Fig. 8a). The area of Xincun Lagoon subsequently reduced further to 21.82 km^2 in 1998, 20.27 km^2 in 2008, and 19.67 km^2 in 2018. Fig. 1 illustrates that variations in the shoreline mainly occurred in the northeastern region of the lagoon, which is dominated by aquaculture activity. The water area of the lagoon was considered to be stable at 22.5 km^2, which is similar to the area of the lagoon reported in the literature (Gong et al., 2004).

4.2. Shoal sandbar

Figs. 8b, c and 9 show the interpretations of the shoal sandbar data from 1962 to 2018. Through the analysis of time series information, it was found that significant temporal and spatial variations have occurred in the shoal sandbars. During 1962–1966, 1973–1980, 1989–1996, and 2000–2016, the shoal sandbar consisted of an ESS and west sand-spit (WSS). The ESS developed as a long strip from east to west, whereas the WSS had an inverted triangle morphology from north to south. However, during 1967–1968, 1986–1988, 1997–1999, and 2017–2018, the presence of an independent MidSS was observed. The area of each part of the shoal sandbar, lengths of the ESS and MidSS (as measured using the longest east–west extent), and length of the WSS (as measured by the longest north–south straight line) were determined and are shown in Figs. 8b, c and 9; notably, the shoal sandbars underwent periodic evolution patterns in different years.

As noted above, the analysis results of the shoal-sandbar time series shown in Figs. 8b, c and 9 indicate that the length of the ESS underwent at least four abrupt shortening processes, which resulted in the creation of a third sandbar: the MidSS. By using the timing of the establishment of a full breach of the ESS, three of these abrupt changes were confirmed to have occurred in 1967, 1997, and 2017, whereas another took place between 1980 and 1986. The exact year of a full breach for this event is uncertain due to the lack of data for the intervening five years. For two of the three older events, the MidSS merged with the WSS within a year. A lack of data between 1968 and 1973 precludes the determination of how much time was required for the MidSS–WSS merger during that episode. Thus, at least four episodes of shoal-sandbar breaching and inlet migration (hereafter 'SB & IM') have occurred in the ebb-tidal delta of Xincun Lagoon since 1962. There were three complete evolution cycles of the shoal sandbar and tidal inlets during the 50-year period from 1967 to 2017. The first two cycles lasted 30 years in total from 1967 to 1997 (an average of 15 years each), while the third cycle lasted 20 years from 1997 to 2017. Therefore, the periods of the evolution cycle of the ebb-tidal delta were different.

Fig. 8c presents a time series that demonstrates the variations in the total area covered by the ESS, MidSS, and WSS. Prior to 2006, the total area of shoal sandbars did not vary significantly from ~0.9 km^2 (except in 2000). Since 2006, the total area of shoal sandbars essentially stabilized within a smaller area of ~0.7 km^2.

4.3. Tidal current channel

The tidal current channels that connect Xincun Lagoon and the offshore region are relatively deep, and are located between (i) the coasts, (ii) the coast and the flood-tidal delta, or (iii) the coast and the ebb-tidal delta. From the chart and inversion depth (Fig. 7), the water depth in the middle section of the ebb-tidal current channel was found to be > 3 m, while that in the entrance section ranged from 1 to 2 m. The length of the main flow curve was used as the length of the channel, as shown in Fig. 1b. The tidal current channel has developed between the northeast terminus of the flood-tidal delta, the inlet throat, and the southwest terminus of the ESS. As the flood-tidal delta is basically stable (Gong et al., 2004; Zhang et al., 1995), the starting points of the flood-tidal current channel were fixed in this study. Thus, the length of the main flood-tidal channel was determined to be 1535 m. Based on the above shoal-sandbar interpretation results, the location, area, and length of the shoal sandbars were found to be in a constant state of flux, whereby their positions determine the end point locations of the ebb-tidal channel. The lengths of the ebb-tidal current channels fluctuated between 650 m and 2300 m. The total tidal channel lengths over time are shown in Fig. 8a.

4.4. Evolution of the shoal sandbar and tidal channel

In Section 4.2, we identified four SB & IM events between 1962 and 2018, and observed that there was a significant periodic evolution in the ebb-tidal delta of Xincun Lagoon. These results confirm the hypotheses of Zhang et al. (1995) and Gong et al. (2004), who used less historical chart data and remote sensing data, respectively, to observe the periodic changes of the tidal inlets in Xincun Lagoon. Four SB & IM events were recognized in the present study, which are denoted as T1 (1967), T2 (mid-1980s), T3 (1997), and T4 (2017). Thus, the entire observation period (1962–2018) could be divided into five cycles: i) the period before 1967 (C1), ii) from 1967 to the mid-1980s (C2), iii) from the mid-1980s to 1997 (C3), iv) from 1997 to 2017 (C4), and v) after 2017 (C5). By analyzing the morphological characteristics of the shoal sandbars at different times in all cycles (Fig. 9), and by referring to the modes of inlet migration and spit breaching as well as incorporating tidal branching and sediment migration modes (summarized by

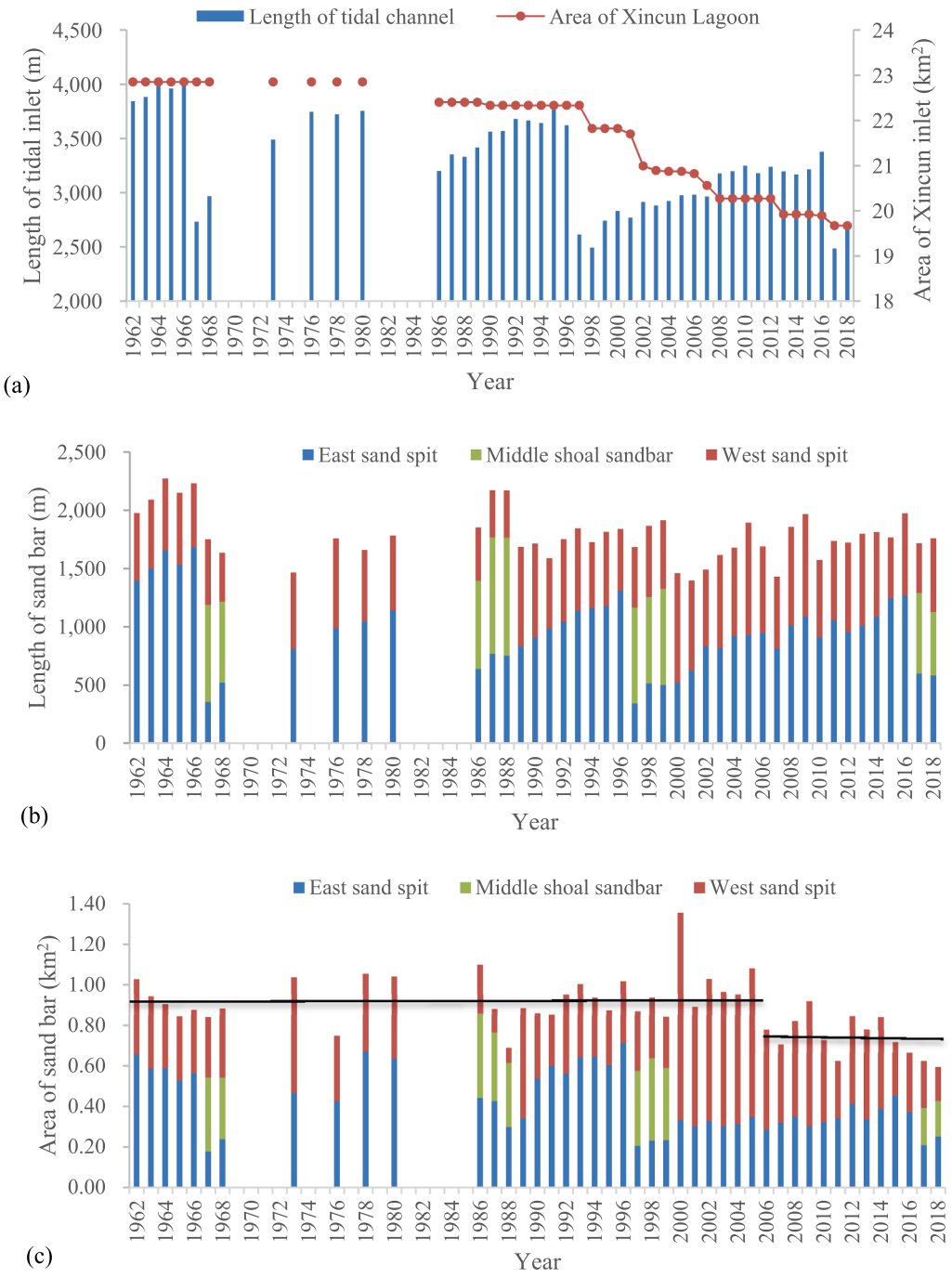

Fig. 8. Time series analysis of Xincun Lagoon characteristics. (a) Length of the tidal channel (blue bars) and area of the lagoon (red circles), (b) length of the shoal sandbar, and (c) area of the shoal sandbar, with separate determinations for the east sand-spit (ESS, blue), middle shoal-sandbar (MidSS, green), and west sand-spit (WSS, red). Black horizontal lines indicate the average area of the shoal sandbar in different periods. (For interpretation of the references to colour in this figure legend, the reader is referred to the web version of this article.)

FitzGerald and Miner (2013)), an evolution cycle was developed and divided into four states. These states include a double-inlet state (S1), a merging and adjustment state (S2), a basic state (S3), and a breaching state (S4) (see Section 5.1). By using these parameters, a summary of the remote sensing observations since 1962 was produced. The results are displayed in Fig. 10, which shows the evolution of the lengths of the ESS during different cycles and the division of the four states in each cycle. Although the number of observations varied in several cycle periods, the lengthening of the ESS exhibited a relatively stable trend, which indicates that the annual observation frequency was sufficient for obtaining reliable observation results over the long period of 15–20 years.

The MCTCs and center points of the CPSPs in each year of C1–C4 are plotted in Fig. 11a–d, which show that the MCTCs extended westwards in each cycle, and that the CPSPs of the ESS moved northwestwards. In Fig. 11b–d, a westward movement of the MidSS occurred for 2–3 years. When the MidSS disappeared, the CPSPs of the WSS suddenly moved eastwards for a long distance, which indicates that the MidSS and WSS merged to form a new WSS. Additionally, in order to further explore the occurrence and development process of SB & IM events while utilizing

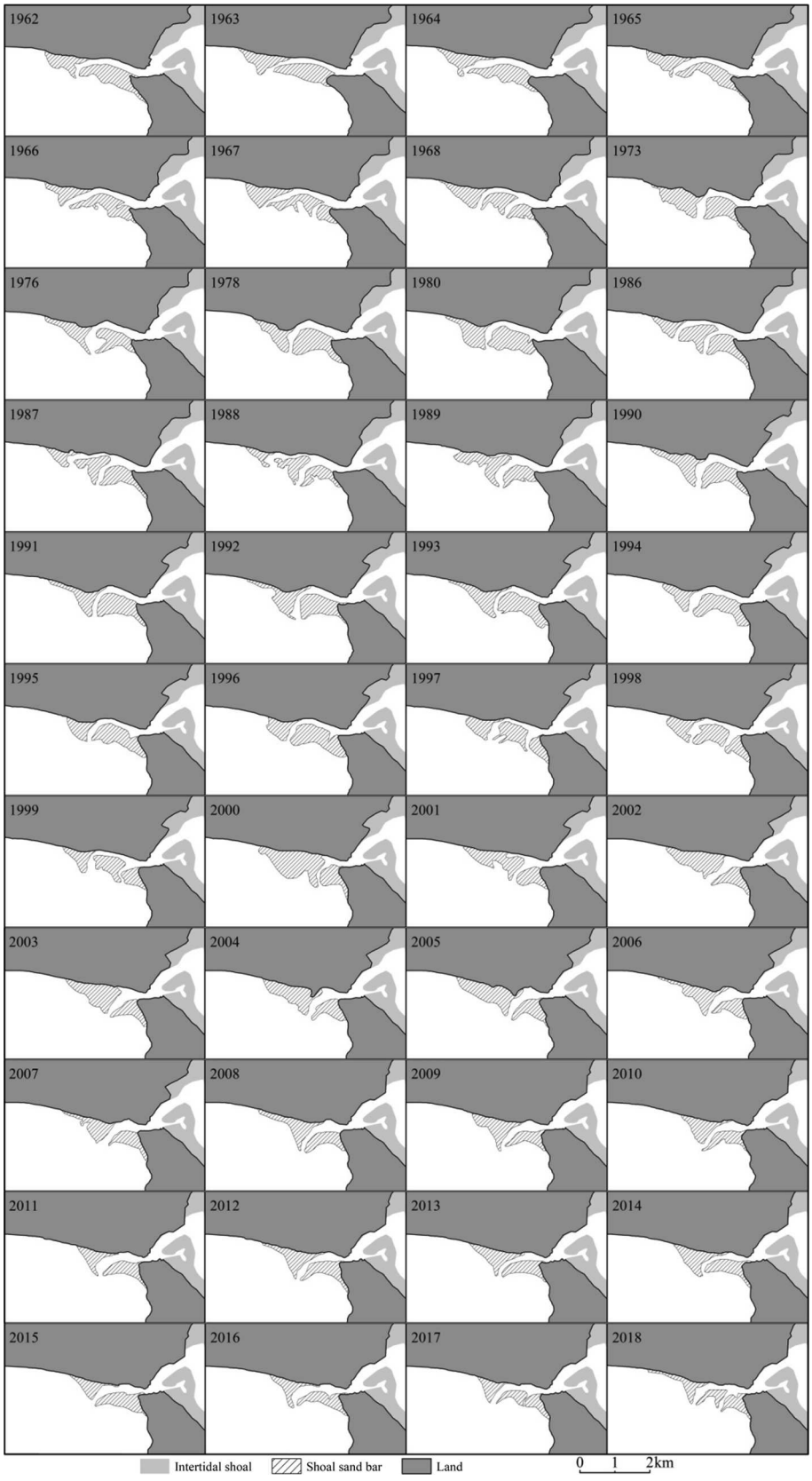

Fig. 9. Shoal sandbar patterns of the ebb-tidal delta at Xincun Lagoon in different years from 1962 to 2018.

the collected satellite data, quarterly observations of the breaching state (S4) of the third and fourth cycles (C3 and C4) were analyzed. These results are shown in Fig. 11e and f, and reveal that the locations of the first breach in the two SB & IM events were close, but the duration of the third breach was longer than that of the fourth one, although the extent of the breach expansion was relatively small.

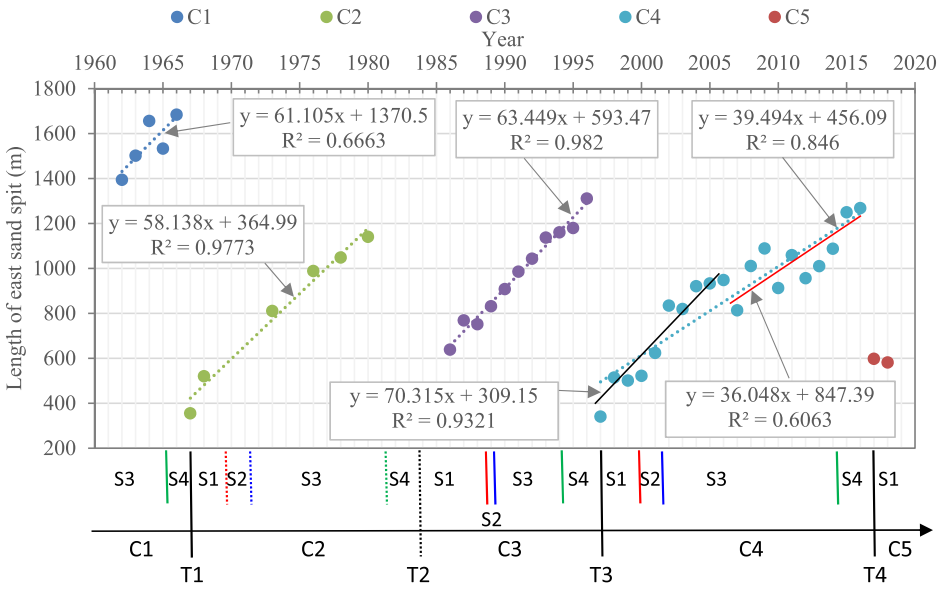

Fig. 10. Time axis division of the cycle periodic evolution and the rate of change of the east sand spit in each cycle.

5. Discussion

5.1. Conceptual model of the ebb-tidal delta evolution

In order to document and understand the periodic evolution process of the ebb-tidal delta in Xincun Lagoon, we performed an in-depth analysis of Figs. 10 and 11, and subsequently developed a conceptual model of the ebb-tidal delta evolution, as illustrated in Fig. 12. This model consists of the four previously mentioned continuous and cyclical states: S1–S4, which are discussed in numeric order corresponding to their simplicity (from low to high).

(S1) Double-inlets state. A complete separation of the ESS into two parts marks the end of one cycle and the beginning of a new cycle. Four such SB & IM events were observed in this study (Fig. 10). In this state, there are two tidal inlets (Fig. 12a) in which the newly formed inlet becomes the main tidal current channel and that of the old channel is weakened, thus promoting an increase in sedimentation. Under the action of a residual current turning seawards on the west side of the main tidal channel and a residual current turning landwards on the east side (Gong et al., 2008), erosion intensifies on the west side of the new channel. A contemporaneous sediment accumulation along the west coast of the new ESS and the MidSS results in their continued westward expansion. The MidSS gradually encroaches on the old tidal channel until the MidSS and WSS merge, at which point, the S1 state is concluded. According to the observation results of the time series (Figs. 6, 8, and 9a–d), the S1 state exists in each cycle, but due to a lack of data, only the fourth cycle had a complete record, which lasted approximately 3 years from 1997 to 2000.

(S2) Merging and adjustment state. Once the MidSS merges with the WSS and the old tidal channel ceases to exist, the merging and S2 state begins. From a certain perspective, this state can be seen as the end of S1 and the beginning of S3, rather than an independent state that lasts a relatively short period of time. However, it is considered that S2 should be retained as an independent state in the conceptual model as a means of showing this adjustment state in more detail, particularly the shape of the east and west shoal-sandbars. After short-term adjustments of the shape of the WSS, the S3 state is established and continues the cyclic evolution process. This state was observed in C3 for ~1 year and in C4 (Fig. 6) for ~2 years.

(S3) Basic state. This state is the most stable in the evolution cycle of the ebb-tidal delta. During this state, the flood tide mainly enters the lagoon along the eastern and southern sides of the tidal channel, whereas the ebb tide returns back to the sea along the northern and western sides, as indicated by the blue arrows in Fig. 12c. To accommodate the constant tidal prism of the lagoon and spit construction, under the influence of tidal inertia and Earth's rotation, erosion occurs along the east side of the WSS and the resultant sediment is transported to the ESS, as described by the seaward dominated flow-field on the west side, and the landward dominated flow-field on the east side (Gong et al., 2008). As a consequence, a contraction of the WSS occurs along its east face, and with the concurrent extension westwards of the ESS and the tidal channel, the inlet is displaced further along the downdrift shoreline (Fig. 11a–d). This state usually persists for the longest duration within the evolution cycle.

(S4) Breaching state. As the ESS continues to extend westward, the tidal channel continues to lengthen and the resistance of the ebb tide increases along with a simultaneous decrease in its velocity (Gong et al., 2004; Zhang et al., 1995). As a result, erosion along the east side of the WSS reduces, as does the suspended sediment transferred to the ESS, especially to the far eastern coast. Erosion of the northern coast near the root of the ESS is shown in Fig. 12d. According to long time-series observations, a critical length of the ESS will eventually be reached, at which time the ebb tide will seek new outlets. Before the first, third, and fourth SB & IM events, the critical length was 1680 m, 1310 m, and 1260 m, respectively. At the critical point, a shoal-sandbar breach will occur near the coast of the ESS outside of the lagoon throat. This action will direct part of the ebb tide towards the gaps, thereby causing stronger erosion and an acceleration of breaching until a complete breach is attained, which marks the end of this cycle. According to our high frequency observations of the third and fourth SB & IM events (Fig. 11e, f), this occurs as a continuous process. For the third SB & IM event (Fig. 11e; T3), no obvious breach was apparent on July 2, 1994, but there was a significant breach in the remote sensing image of October 22, 1994. This indicates that the critical point was reached between these two dates. Analysis of the sandbar boundary conditions in Fig. 11e indicates that the breach continued to widen until a complete breach was attained on (or within several weeks prior to) August 27, 1997. The time from the initial erosion of the breach channel to the complete breach approached 3 years. Similarly, in the fourth SB & IM event (Fig. 11f; T4), the breaching process lasted just under 2 years. The

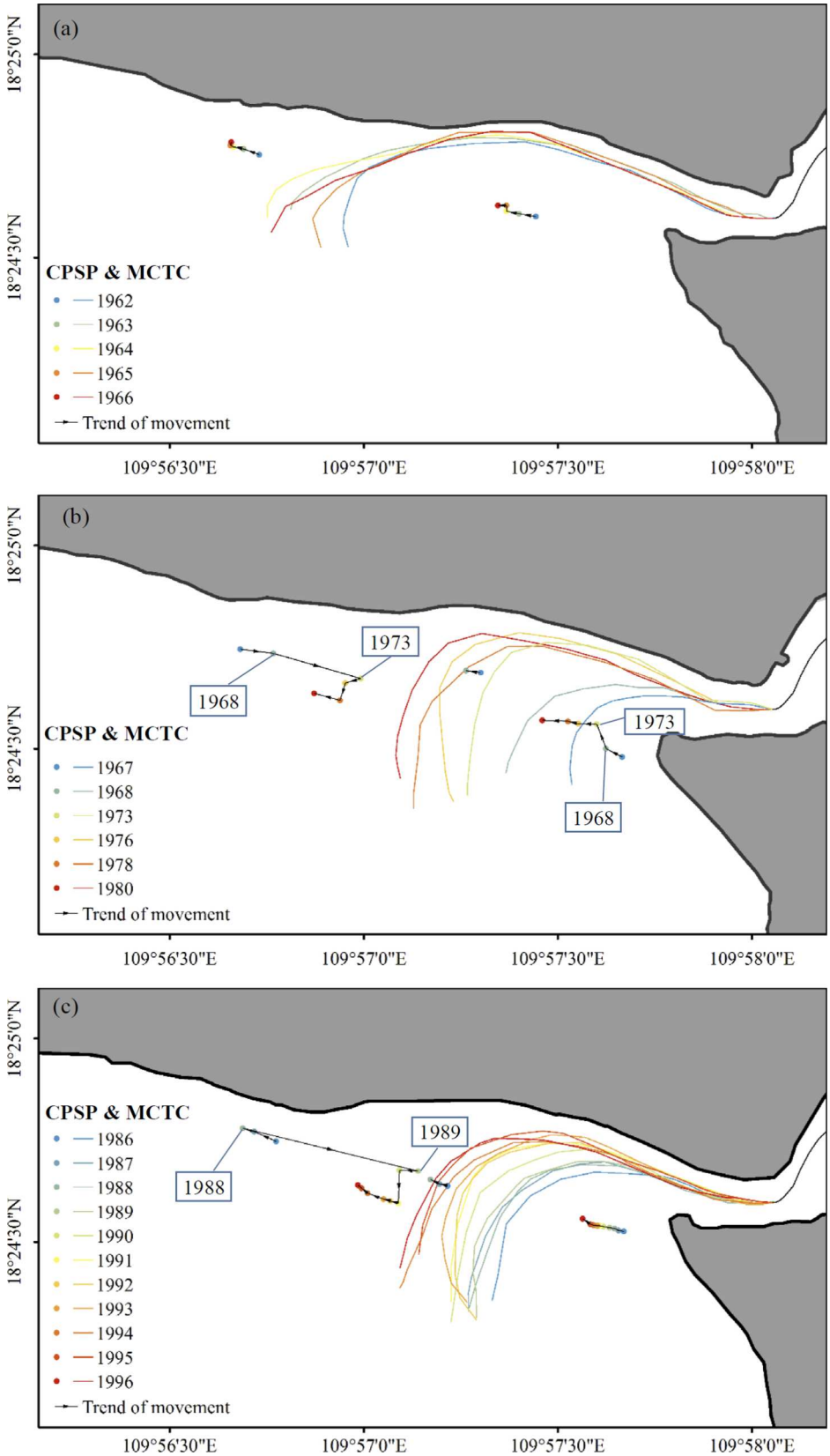

Fig. 11. Main current curves of the tidal current channels (MCTCs, represented by the dots) and the center point of shoal-sandbar patches (CPSPs, represented by the lines) of the cycles (C): (a) C1, (b) C2, (c) C3, and (d) C4, where the dot and line colors refer to different years. The boundary variation of the shoal-sandbar breaching and inlet migration events are shown for (e) C3 and (f) C4, where the line colors refer to different dates (year/month/day). (For interpretation of the references to colour in this figure legend, the reader is referred to the web version of this article.)

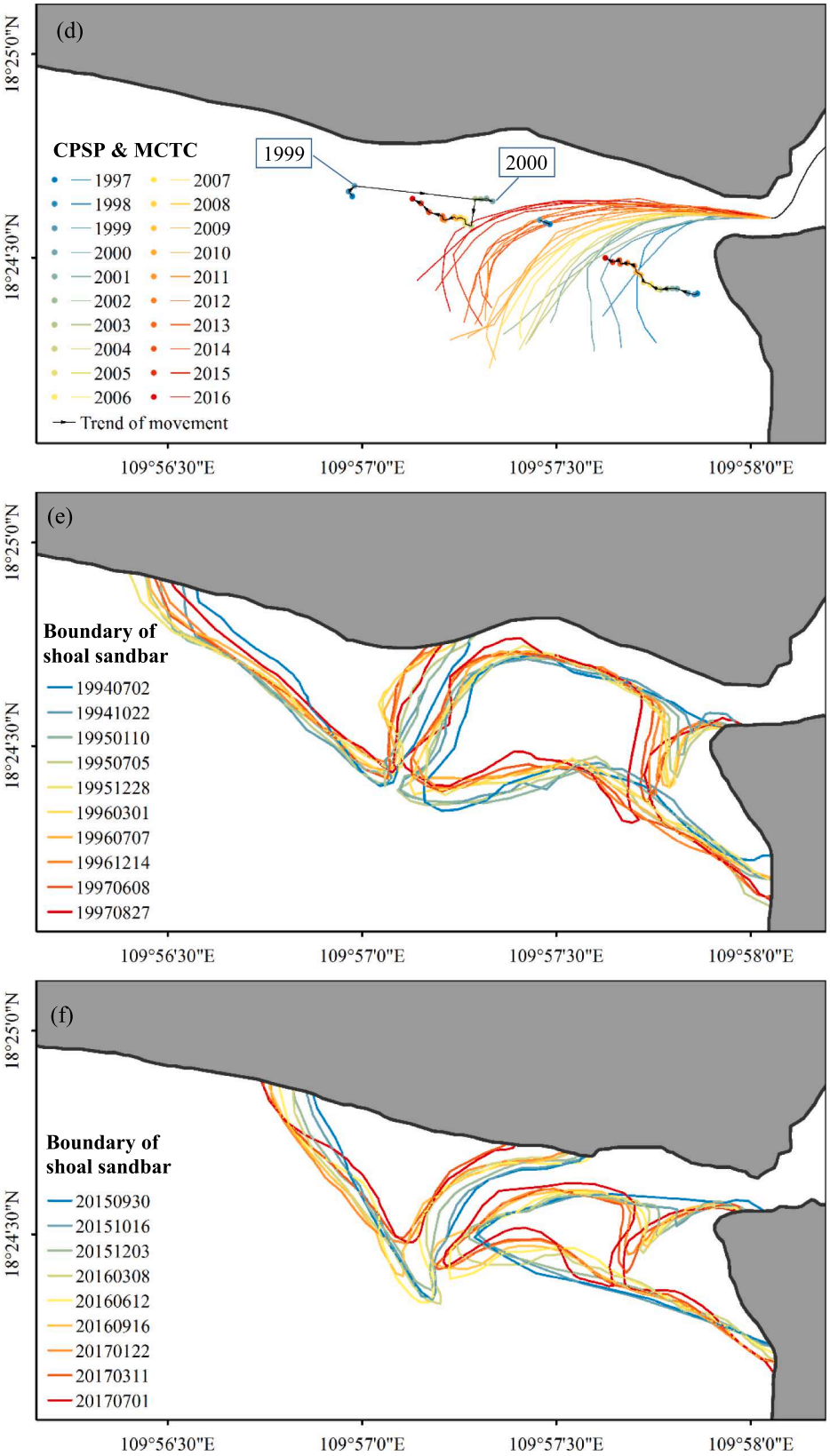

Fig. 11. (*continued*)

initial breach for T4 was first found on October 16, 2015, and it continued to expand until total breaching on or before July 1, 2017. The occurrences during this period are discussed in Section 5.2.

5.2. Long-term cycle for the periodic evolution of the ebb-tidal delta

The previous observations and conceptual model analysis based on long time-series remote sensing data revealed that the period of long-

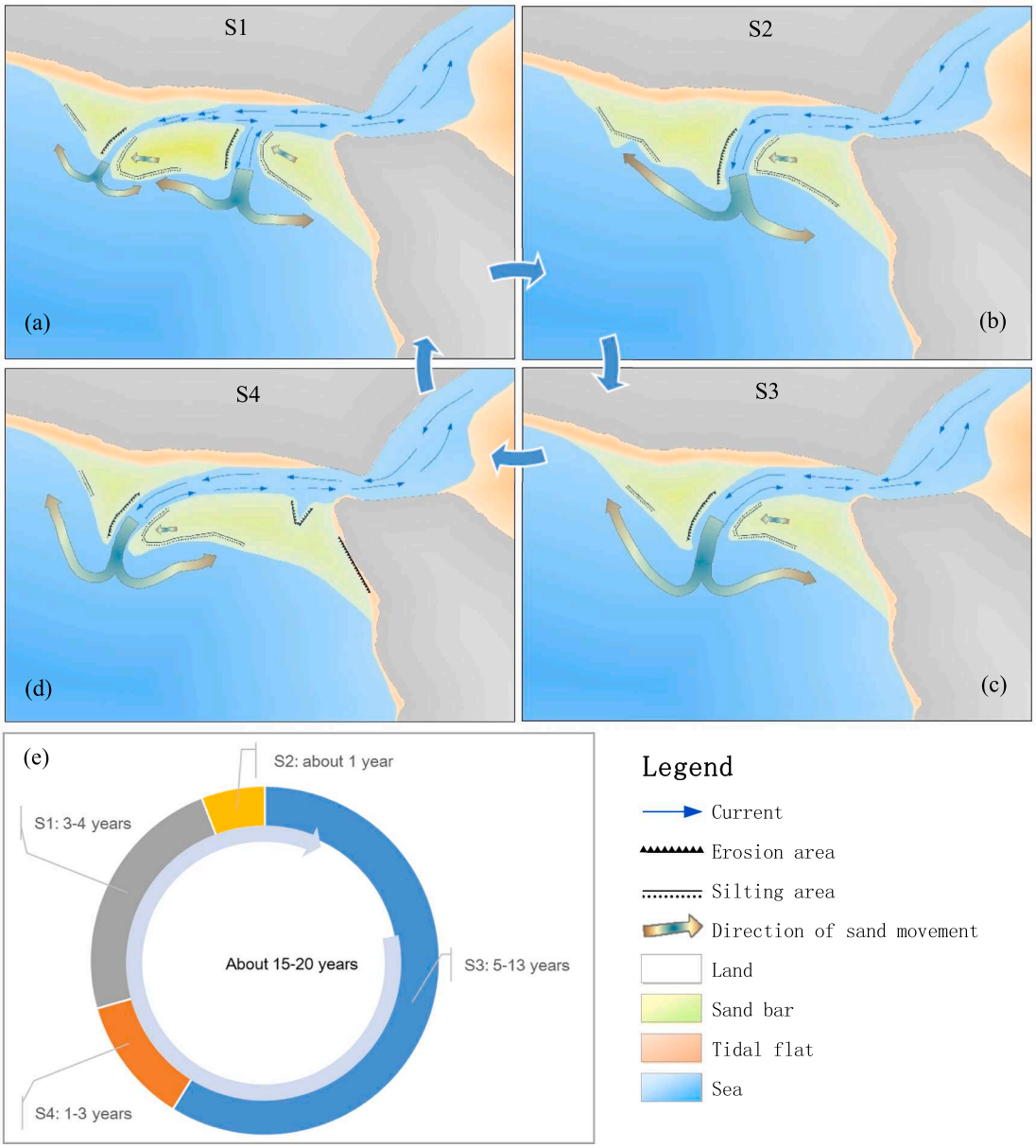

Fig. 12. Conceptual model for the cyclical evolution of the ebb-tidal delta of Xincun Lagoon. (a) Double-inlets state (S1), (b) merging and adjustments state (S2), (c) basic state (S3), and (d) breaching state (S4). (e) Representation of the temporal cyclical changes at Xincun Lagoon.

term cyclic evolution of the ebb-tidal delta in Xincun Lagoon is approximately 15–20 years, which includes all four states (S1–S4). An important scientific question that needs to be answered urgently is: what is the key factor causing this long-term cycle for the periodic evolution?

Seabed friction is known to play an important role in shallow water environments, especially for the evolution of tidal channels (FitzGerald and Miner, 2013; Gaudiano and Kana, 2001; Gong et al., 2004; Zhang et al., 1995). Although we did not measure seabed friction, hypothetically, an increase in the tidal channel length makes the effect of seabed friction more significant. As a result, the exchange of water between the outside sea and the lagoon will be retarded, and in turn, the currents in the entrance tidal channel will be reduced. Therefore, after sufficient time, the ESS and tidal channel will both become long enough such that the seabed friction of the tidal channel will be very significant, which can seriously affect the water exchange between the outside ocean and Xincun Lagoon. When there is a storm during this condition, under the influence of heavy rainfall and storm waves, the water level of lagoon will rise abnormally, but the water cannot be discharged to the outside ocean through the long tidal-channel in time. Consequently, a new breach should be generated in a suitable location to discharge the large amount of water in the lagoon. In this study of Xincun Lagoon, the length of the sandbar increased by between 36 and 70 m each year (Fig. 10), and the periods of the four cycles were estimated as probably being between 15 and 20 years.

Xincun Lagoon is a typical coastal lagoon–tidal inlet system. From the perspective of its structural form with a medium-sized coastal lagoon and slender tidal channel, it is also a typical Helmholtz resonance system. Moreover, resonance is a ubiquitous phenomenon in nature. Therefore, we believe that Helmholtz resonance may be another important factor affecting the long-period evolution of the ebb-tidal delta.

The Helmholtz resonance model was thus employed to analyze the stability of the tidal inlets and shoal sandbars at Xincun Lagoon. The Helmholtz resonance frequency and period were calculated without considering the damping effect. According to Eqs. (1) and (2), the tidal channel length (L) and lagoon area (S) in the time series were obtained

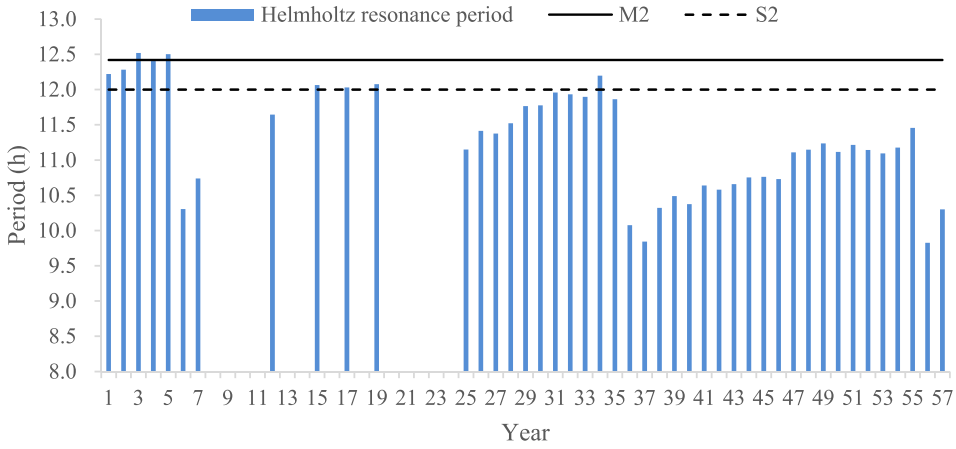

Fig. 13. Helmholtz resonance period (blue bars) for Xincun Lagoon. The black solid and dashed lines are the periods of the M2 and S2 harmonic constituents, respectively. (For interpretation of the references to colour in this figure legend, the reader is referred to the web version of this article.)

from remote sensing images. The depth and width of the tidal channel in Xincun Lagoon are relatively stable (Gong et al., 2004). The analysis of chart data surveyed in 2014 revealed that the tidal channel at the estuary was shallow (1.4 m deep). The width of the tidal channel, defined as the distance between the ESS and WSS at the estuary, was found to be 120 m. Therefore, by using these parameters, we calculated the time series of the Helmholtz resonance period (converted into hours), which fluctuated between 9.1 and 12.7 h (Fig. 11). According to Yang et al. (2016b), the tide in Xincun Lagoon is mainly an irregular full-day mixed tide with contributions from the four main harmonic constituents as follows: O1 (with a period of 25.82 h), K1 (with a period of 23.93 h), M2 (with a period of 12.42 h), and S2 (with a period of 12 h). Thus, the periods of M2 and S2 are similar to those of the Helmholtz resonance period, and these are also plotted in Fig. 13.

Fig. 13 shows that Helmholtz resonance period exhibited periodic variations that were identical to those of the lengths of the tidal current channel and the ESS. Compared with Fig. 8, on the eve of the first, second, and third SB & IM events, Helmholtz resonance period exceeded the periods of M2 and S2. However, on the eve of the fourth SB & IM event, the value of the Helmholtz resonance period was ~ 11.5 h, which was lower than that of M2 and S2 by 0.5–1.6 h. It can be seen that when SB & IM events occur in the ebb-tidal delta of Xincun Lagoon, the Helmholtz resonance period reaches or approaches the periods of M2 and S2. That means Xincun Lagoon is likely to generate tidal resonance at this time. Prandle and Rahman (1980) suggested that tidal resonance can increase the amplitude of tidal waves sharply and increase the tidal level difference between a lagoon and the sea. Mullarney et al. (2008) proposed that Helmholtz resonance in coves results not only in an increased water level difference, but also increases the flow velocity at the tidal channel entrance. An increased water level difference between the lagoon and the offshore coupled with an increased flow velocity at the lagoon entrance further enhance the instability of shoal sandbars in an ebb-tidal delta. As for Xincun Lagoon, its ebb-tide delta is more prone to experience shoal-sandbar breaching. Therefore, Helmholtz resonance is an important factor for SB & IM in the ebb-tidal delta in Xincun Lagoon.

By using the above analysis in combination with the results of previous studies (Gong et al., 2004; Zhang et al., 1995), the long-term evolution of the ebb-tide delta in Xincun Lagoon can be summarized as a conceptual model (Fig. 14). A westward extension of the ESS is accompanied by (1) an extension and increase in the resistance of the tidal channel due to the effect of friction, which subsequently reduces the current in the tidal channel and increases the water level difference at the lagoon throat (Gong et al., 2004; Zhang et al., 1995), especially during flood conditions, and (2) an increase in the Helmholtz resonance period in the lagoon that may reach or approach M2 and S2, thus significantly increasing the water level difference at the tidal inlet during a storm-surge. The combined effect of the two factors leads to a larger water level difference between the ocean and lagoon, even to that exceeding the required threshold of water level difference for breaching, which makes shoal sandbars highly susceptible to breaching, particularly during storms (FitzGerald and Miner, 2013). As shown in Fig. 10, during the T1 (1967), T3 (1997), and T4 (2017) SB & IMs events, the length of the ESS was 1684 m, 1311 m, and 1268 m, respectively. Therefore, the threshold of tidal channel length as breaching in Fig. 14, might be about 1200 m.

5.3. Short-term process of shoal sandbar breaching

According to the high-frequency tracking observations of breaching processes (S4) during the third and fourth SB & IM events in Fig. 11e and f, both initial breaches occurred during the autumn. Zhang et al. (1995) and Gong et al. (2004) both pointed out that the tidal inlet migration in the ebb-tidal delta of Xincun Lagoon could be triggered by sudden events such as typhoon storms, rainstorms, and floods on the basis of the extension of the tidal channel. This is similar to the reason given for inlet migration and barrier island breaching by FitzGerald and Miner (2013). In order to analyze the short-term process of SB & IM in the ebb-tidal delta of Xincun Lagoon, we collected precipitation data, typhoon data, wind data, and wave data (as described in Section 2.3), which are presented in Fig. 15 for the third and fourth SB & IM events in 1994 and 2015.

As can be seen from Fig. 15, the typhoons were usually accompanied by heavy precipitation, strong winds, and high SWHs. In addition, multiple typhoons, including No. 199400, No. 199418, No. 199422, No. 199423, and No. 201522, also exhibited sudden changes in the wind and wave directions from southwest to northeast, which were basically the same as that of the ebb tide in the tidal inlet of Xincun Lagoon. Fig. 15a and c present the data for the 1994 SB & IM event, whereby the imaging times of the two remote sensing images indicate that the first breach occurred between July 2 and October 22. During this period, five typhoons affected Xincun Lagoon, and the last three caused heavy precipitation. Fig. 15b and d display the data for the SB & IM event in 2015, when the first breach occurred between September 30 and October 16 (i.e., the time between the two remote sensing images). One typhoon (No. 201522) affected Xincun Lagoon during this period and resulted in a large amount of cumulative rainfall and a significant increase in the SWH and wind speed. These results indicate that there were typhoon storm-surges before the first breach of both of these SB & IM events, which is also consistent with the existing understanding of SB & IMs (FitzGerald and Miner, 2013; Gong et al., 2004; Zhang et al., 1995).

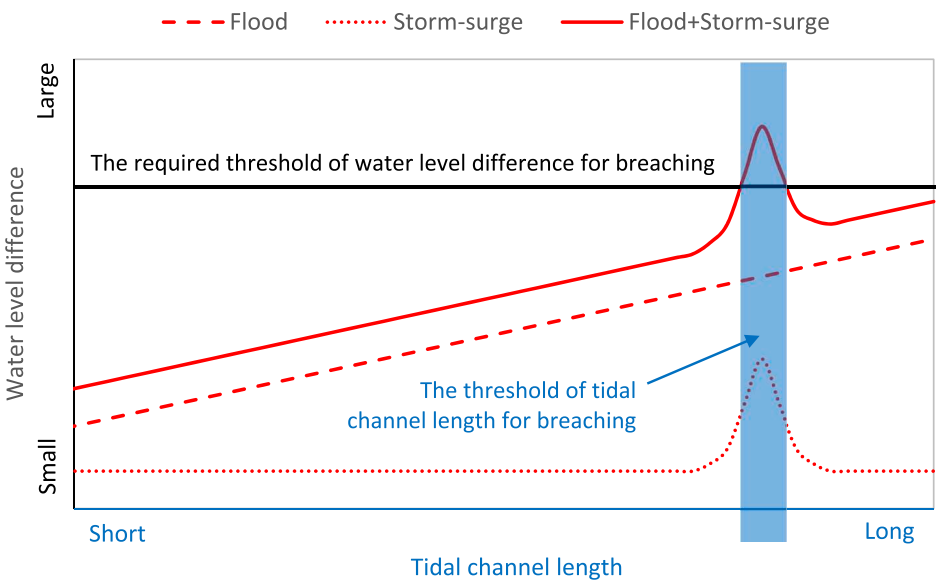

Fig. 14. Conceptual model for qualitatively describing the water level difference increase due to a flood and/or storm-surge. The black solid line represents the required threshold of water level difference for breaching, and blue columns are the threshold of tidal channel length as breaching. (For interpretation of the references to colour in this figure legend, the reader is referred to the web version of this article.)

On the basis of Fig. 15, it can be found that the changes in the wind and waves during the typhoons before the two breaches in 1994 and 2015 shared a common feature; the wind direction and wave direction in the area of Xincun Lagoon suddenly reversed from southwest to northeast under the influence of the typhoons. We particularly noticed the typhoons that affected Xincun Lagoon in September (No. 201519) and October 2015 (No. 201522), whereby that in September was accompanied by heavier precipitation, stronger winds, and higher SWHs in comparison to the October typhoon, and yet a breach did not occur in September. The difference between these two typhoons is whether the wind and wave direction changed significantly. Does this mean that wind and wave directions play important roles in triggering breaches in areas affected by heavy rainfall and strong waves? Fisher pointed out that the breaching process is enhanced when offshore winds accompany the ebbing tide. Sudden changes in wind and wave directions may be favorable factors for disturbing the hydrodynamics and sand conditions of the shoal sandbar. Under the high water level conditions brought by a storm-surge and heavy rainfall, and accompanied by strong winds and waves along the ebb-tide direction, the storm-surge elevated waters and waves will enhance the speed of the ebbing tide across the shoal sandbar, overwash the shoal sandbar, and then destroy the foredune ridge of the sandbar. Although this initial breach process may produce a small and shallow overwash channel from the tidal channel side, the breach mouth will continue to expand and deepen until the shoal sandbar is completely cutoff. According to Fig. 11e and f, this breaching state (S4) will last for 1–2 years. Therefore, the SB & IM events observed in Xincun Lagoon were affected both by typhoon storm-surges and the corresponding heavy rainfall, strong winds, and high waves. In addition, the wind direction and wave direction also played very important roles. Breaching is more easily triggered when the ebbing tide current is accompanied by strong winds and waves in the same direction.

5.4. Remote sensing monitoring and warning of periodic evolution of the ebb-tidal delta

The previous discussion demonstrated that the periodic evolution of the ebb-tidal delta is mainly manifested by the periodic changes of the ESS and tidal channels. According to Fig. 10, four SB & IM events occurred between 1962 and 2018, and these included three complete evolution cycles, namely, C2, C3, and C4. Due to the lack of observation data between 1980 and 1985, the individual period lengths of C2 and C3 could not be determined explicitly; however, the total length of these two cycles was 30 years. Therefore, it was estimated that the period length of each cycle was approximately 15 years, while that of C4 was 20 years, which means that there were differences in the evolutionary cycle of each period. In detail, we analyzed the characteristics of the westward extension of the ESS in different cycle periods, as shown in Fig. 10. During the T1 (1967), T3 (1997), and T4 (2017) SB & IMs events, the length of the ESS was 1684 m, 1311 m, and 1268 m, respectively. During the C1 (1962–1966), C2 (1967–mid-1980 s), C3 (mid-1980s–1996), and C4 (1997–2016) cycles, the rate of lengthening of the ESS was 61.1 m/a (R^2 = 0.6663), 58.1 m/a (R^2 = 0.9773), 63.4 m/a (R^2 = 0.9820), and 39.5 m/a (R^2 = 0.8460), respectively. Hence, the rate of lengthening of the ESS during the C4 cycle was considerably lower than that of the previous periods. By carefully analyzing the length data for the ESS in the C4 cycle, it was concluded that a significant event(s) occurred in 2006, which resulted in a major decrease in this parameter. If the data before 2006 are considered separately, the rate of lengthening of the ESS for that time period was 70.3 m/a (R^2 = 0.9321), which is close to or greater than that in the previous three cycles. However, after 2007 this rate was obviously lower at only 36.0 m/a with a larger volatility (R^2 = 0.6060). To summarize, from 1962 to 2006, the rate of lengthening of the ESS ranged from 58.1 to 70.3 m/a with a high stability (as indicated by high correlation coefficients), whereas it decreased significantly after 2006.

It can be seen that the length and rate of lengthening of the ESS are important parameters to characterize the ebb-tidal delta. By using sufficiently long time-series remote sensing data, the length and its corresponding variation characteristics of the ESS can be obtained. In turn, combined with the evolution model of ebb-tidal delta (e.g., the conceptual model proposed in Section 5.1), the trend of the ESS can provide early warning of the occurrence of SB & IM events (Fig. 14). Therefore, by drawing on the advantages of time-series remote sensing analysis and by selecting relevant morphological parameters (e.g., the length of the ESS or the tidal channels as index parameters), it is both feasible and valuable to establish a monitoring and early warning framework of the evolution of ebb-tidal deltas based on remote sensing.

6. Conclusions

The majority of changes to the ebb-tidal delta analyzed in this study can be attributed to tidal inlet processes; hence, an understanding of these processes is important to effectively manage the systems of Xincun Lagoon. In this study, based on 153 remote sensing images obtained for the period 1962–2018, we described the decadal (~15–20 years) periodic evolution characteristics of the ebb-tidal delta

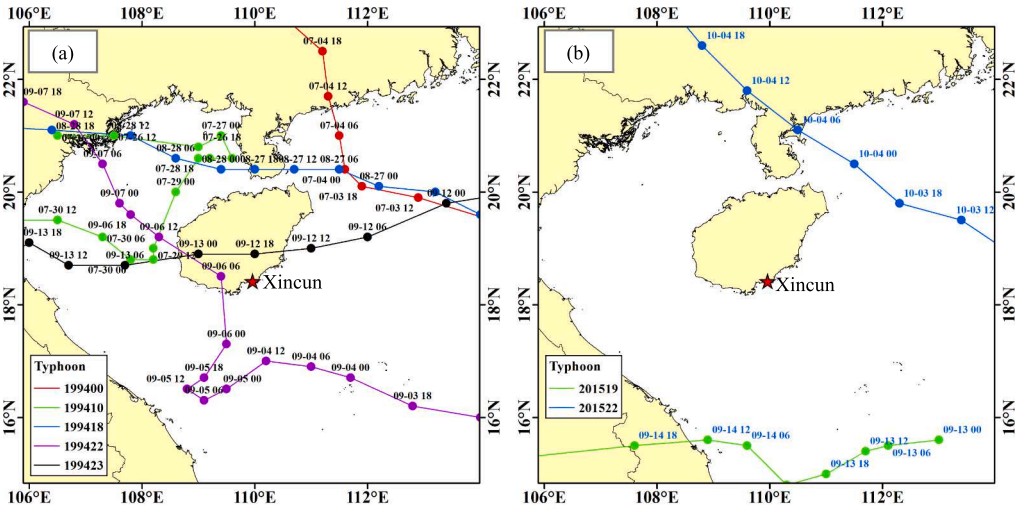

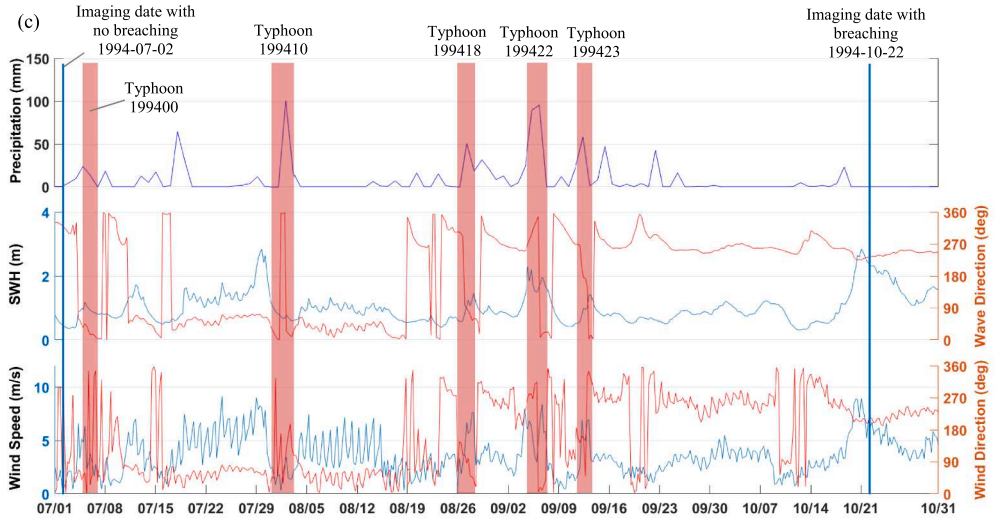

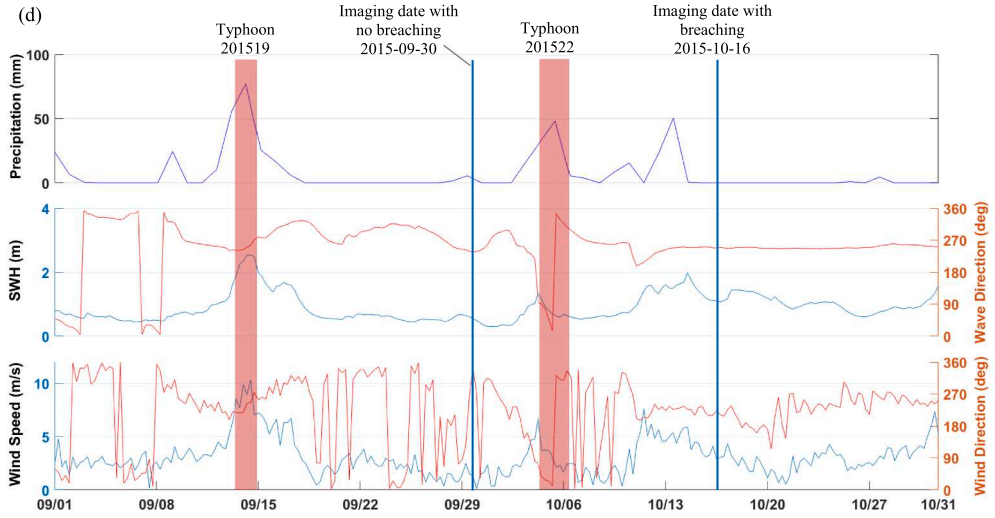

Fig. 15. Typhoon, precipitation, wind speed, and wave information during two breaching events. (a) Typhoons and path information that affected Xincun Lagoon before and after the breaching event in 1994. During the two remote sensing observations, there were five typhoons that affected Xincun Lagoon. (b) Typhoons and path information that affected Xincun Lagoon before and after the breaching event in 2015; there were two typhoons, one of which occurred between the two remote sensing observations. (c) Precipitation, wind speed, and wave data for the period from July 1 to October 31, 1994, and the typhoons (red columns) corresponding to the display in (a); the time of the two remote sensing observations are marked (blue straight lines). (d) Precipitation, wind speed, and wave data for the period from September 1 to October 31, 2015, and the typhoons (red columns) corresponding to the display in (b); the time of the two remote sensing observations are marked (blue straight lines). (For interpretation of the references to colour in this figure legend, the reader is referred to the web version of this article.)

of Xincun Lagoon, and presented a conceptual model of the periodic evolution of the ebb-tidal delta. Then, we discussed the long-term periodic evolution, short-term process, and triggering factors of shoal breaching based on historical typhoons and precipitation, wind, and wave data. The primary results obtained are as follows:

(1) Four SB & IM events in 1967, the mid-1980s, 1997, and 2017, as well as the corresponding periodic variations of the ebb-tidal delta, were observed. Based on the analysis of the time-series variation characteristics of the shape and area of the shoal sandbar as well as the spatial position and length of the tidal current channel, a conceptual model of the periodic evolution of the ebb-tidal delta was

proposed. The model divides the entire evolution period into four progressive stages: the double-inlet state (S1), merging and adjustment state (S2), basic state (S3), and breaching state (S4). The model explains the periodic evolution process of the shoal sandbar and tidal inlets in the ebb-tidal delta of Xincun Lagoon. The model can also be viewed as a typical case for shoal-sandbar evolution following the model of inlet migration and barrier island breaching summarized by FitzGerald and Miner (2013). The decadal cyclical evolutions reported in this study highlight that Xincun Lagoon provides a perfect case study area for evaluating the formation and evolution mechanisms of tidal inlets and the sedimentary bypassing of ebb-tidal deltas.

(2) In addition to the effect of seabed friction, Helmholtz resonance was introduced as another important controlling factor for the long-term periodic evolution of the ebb-tidal delta in Xincun Lagoon. The continuous extension of the ESS of the ebb-tidal delta of Xincun Lagoon leads to the synchronous westward extension of the tidal channel, which further strengthens the effects of seabed friction in the tidal channel and Helmholtz resonance in the lagoon. When the ESS and tidal channel are long enough, the effects of seabed friction and semidiurnal Helmholtz resonance both become significant. These effects severely hinder the water exchange between the lagoon and the open ocean, and in turn increase the corresponding water level difference. This represents an important prerequisite for the occurrence of SB & IM events, particularly during storms (FitzGerald and Miner, 2013).

(3) Based on historical data for typhoons, precipitation, winds, and waves, the short-term processes of the SB & IM events in 1994 and 2015 were analyzed. It was confirmed that during the short period before these two SB & IM events, Xincun Lagoon was affected by typhoons and the accompanying heavy rainfall, strong winds, and high waves. Under the high water level conditions that follow such a storm-surge and the accompanying heavy rainfall, strong winds, and waves along the ebb-tide direction, the elevated waters and waves will (i) enhance the speed of the ebbing tide across the shoal sandbar, (ii) overwash the shoal sandbar, and (iii) then destroy the foredune ridge of the sandbar. This work shows that storm-surge and heavy rainfall are the key factors that trigger the occurrence of SB & IM events. In addition, the wind direction and wave direction also play very important roles. Breaching is more easily triggered when the ebbing tide current is accompanied by strong winds and waves in the same direction. Although this initial breaching process may produce a small and shallow overwash channel, the breach mouth will continue to expand and deepen until the shoal sandbar is completely cutoff over the next 1–2 years.

In summary, the long-period evolution process of the ebb-tidal delta in Xincun Lagoon is controlled by the effects of seabed friction and lagoon resonance. The length of time depends on the extension speed of the ESS. According to the observations in this study, the evolution period of the ebb-tidal delta in Xincun Lagoon is 15–20 years. In terms of the short-term process of breaching, the shoal sandbar in the ebb-tidal delta is jointly triggered by typhoon storm-surges and the accompanying heavy rainfall, strong winds, and strong waves. It is also affected by the synchronized wind direction, wave direction, and tide conditions. It can be seen that the periodic evolution process of the ebb-tidal delta in Xincun Lagoon is a systematic process controlled or influenced by many factors. At the same time, this study shows that changes in the length of the ESS or the length of the tidal channel can be used as a significant early warning indicator for SB & IM events. It is both feasible and valuable to establish a monitoring and early warning framework of ebb-tidal deltas based on remote sensing. The length of the ESS should be monitored on a frequent basis as part of the coastal zone safety management of Xincun Lagoon. Once the ESS reaches a certain length (e.g., 1000 m), manual excavation could be carried out to induce SB & IM events prior to unpredictable events, thus maintaining some degree of stability in the tidal channel. In addition, the long time-series data and conceptual model of the periodic evolution of the ebb-tidal delta proposed in this study can also provide support and validation data for further field observations and numerical modeling research based on hydrodynamic processes, sedimentary processes, and coastal wave processes, to aid the reconstruction of the ebb-tidal delta evolution and deepen the understanding of its mechanism.

Declaration of Competing Interest

The authors declare that they have no known competing financial interests or personal relationships that could have appeared to influence the work reported in this paper.

Acknowledgements

The authors wish to acknowledge OSU Tidal Prediction Software (OTPS) (developed by Gary D. Egbert and Svetlana Y. Erofeeva from Oregon State University, and downloaded from http://volkov.oce.orst.edu/tides/) for the estimations of the tidal level corresponding to the imaging time of each scene. The remote sensing images from Landsat-1/3/5/8 and Keyhole-4/9 were obtained from https://www.usgs.gov. The HJ-1A/1B data used in this article were provided by the China Center for Resources Satellite Data and Application. The precipitation data used in this paper were obtained from the Tropical Rainfall Measuring Mission (TRMM, downloaded from http://trmm.gsfc.nasa.gov). This research was supported by the National Key Research and Development Program of China (grant number 2018YFC1407200), the National Natural Science Foundation of China (grant numbers 41876208, 41830540, and 41576174), the Scientific Research Fund of the Second Institute of Oceanography, Ministry of Natural Resources of China (grant number JT1703), and a project of the State Key Laboratory of Satellite Ocean Environment Dynamics, Second Institute of Oceanography, Ministry of Natural Resources of China (grant number SOEDZZ1803). The authors would like to thank Dr. Yining Chen for her comments on this paper and Editage for editing and reviewing this paper for English language style conventions.

References

Alesheikh, A.A., Ghorbanali, A., Nouri, N., 2007. Coastline change detection using remote sensing. Int. J. Environ. Sci. Technol. 4 (1), 61–66.

Alpers, W., Hennings, I., 1984. A theory of the imaging mechanism of underwater bottom topography by real and synthetic aperture radar. J. Geophys. Res. 89 (C6), 10529–10546. https://doi.org/10.1029/JC089iC06p10529.

Chen, B.Q., Yang, Y.M., Xu, D.W., Huang, E.H., 2019. A dual band algorithm for shallow water depth retrieval from high spatial resolution imagery with no ground truth. J. Photogram. Remote Sens. 151, 1–13. https://doi.org/10.1016/j.isprsjprs.2019.02.012.

Engenio, F., Marcello, J., Martin, J., 2015. High-resolution maps of bathymetry and benthic habitats in shallow-water environment using multispectral remote sensing imagery. IEEE Trans. Geosci. Remote Sens. 53 (7), 3539–3549. https://doi.org/10.1109/TGRS.2014.2377300.

FitzGerald, D.M., Miner, M.D., 2013. Tidal inlets and lagoons along siliciclastic barrier coasts. In: Shroder, J. (Editor in Chief), Sherman, D.J. (Ed.), Treatise on Geomorphology, Academic Press, San Diego, CA. Coastal Geomorphol., 10, 149–165.

Guo, H., Liu, J., Li, A., Zhang, J., 2012. Earth observation satellite data receiving, processing system and data sharing. Int. J. Digital Earth 5, 241–250. https://doi.org/10.1080/17538947.2012.669963.

Garel, E., Sousa, C., Ferreira, O., Morales, J.A., 2014. Decadal morphological response of an ebb-tidal delta and down-drift beach to artificial breaching and inlet stabilization. Geomorphology 216, 13–25. https://doi.org/10.1016/j.geomorph.2014.03.031.

Garrett, C., 1972. Tidal resonance in the Bay of Fundy and Gulf of Maine. Nature 238, 441–443.

Gaudiano, D.J., Kana, T.W., 2001. Shoal bypassing in mixed energy inlets: geomorphic variables and empirical predictions for nine South Carolina inlets. J. Coastal Res. 17 (2), 280–291.

Gong, W.P., Shen, J., Chen, B., 2007. Obtaining water elevation in the lagoon and cross-sectionally averaged velocity of the tidal inlet by using one-dimensional hydraulic equation—A case study in Xincun Inlet Linshui, Hainan, China. J. Oceanograp. Taiwan Strait 26 (3), 301–313.

Gong, W.P., Chen, M.H., Wen, X.J., Mo, J.S., 2004. Evolution and stability of Xincun tidal inlet, Linshui County, Hainan Province. J. Trop. Oceanography 23 (4), 25–32.

Gong, W.P., Wang, D.R., 2006. Stability analysis and equilibrium area calculation of tidal inlet—A case study in Xincun inlet, Linshui, Hainan Island. J. Trop. Oceanography 25 (4), 31–41.
Gong, W.P., Wang, Y.P., Wang, D.R., Chen, B., 2008a. Hydrodynamics under combined action of wave and tide and its implication for the sediment dynamics in Xincun tidal inlet, Hainan. J. Marine Sci. 26 (2), 1–12.
Gong, W.P., Shen, J., Wang, D.R., 2008b. Mean water level setup/set down in the inlet-lagoon system induced by tidal aetion–A case study of Xincun inlet, Hainan Island in China. Acta Oceanolog. Sin. 27 (5), 63–80.
Greenberg, D.A., 1979. A numerical model investigation of tidal phenomena in the Bay of Fundy and Gulf of Maine. Mar. Geod. 2 (2), 161–187.
Hayes, M.O., 1980. General morphology and sediment patterns in tidal inlets. Sed. Geol. 26, 139–156.
Herrling, G., Winter, C., 2014. Morphological and sedimentological response of a mixed-energy barrier island tidal inlet to storm and fair-weather conditions. Earth Surf. Dyn. 2, 363–382.
Jiang, Z.J., Fang, J.G., Zhang, J.H., Gu, Z.F., Wang, W., Wang, A.M., 2009. The calculation of tidal water capacity and water exchange characteristic of Li'an lagoon. Natural Sci. J. Hainan Univ. 27 (3), 261–264.
Karsli, F., Guneroglu, A., Dihkan, M., 2011. Spatio-temporal shoreline changes along the southern Black Sea coastal zone. J. Appl. Rem. Sens. 5 (1), 053545. https://doi.org/10.1117/1.3624520.
Lee, Z., Carder, L.K., Mobley, C.D., Steward, R.G., Patch, J.S., 1998. Hyperspectral remote sensing for shallow waters. I. A semi-analytical model. Appl. Opt. 37 (27), 6329–6338.
Li, L., Huang, X.P., 2012. Three tropical seagrasses as potential bioindicators to trace metals in Xincun Bay Hainan Island, South China. Chin. J. Oceanol. Limnol. 30 (2), 212–224.
Li, W., Gong, P., 2016. Continuous monitoring of coastline dynamics in western Florida with a 30-year time series of Landsat imagery. Remote Sens. Environ. 179, 196–209.
Lyzenga, D.R., 1977. Reflectance of a flat ocean in the limit of zero water depth. Appl. Opt. 16 (2), 282.
Maas, L.R.M., 1997. On the nonlinear Helmholtz response of almost-enclosed tidal basins with sloping bottoms. J. Fluid Mech. 349, 361–380.
Mason, D.C., Davenport, I.J., Robinson, G.J., Flather, R.A., McCartney, B.S., 1995. Construction of an inter-tidal digital elevation model by the 'Waterline'Method. Geophys. Res. Lett. 22, 3187–3190. https://doi.org/10.1029/95GL03168.
Mason, D.C., Scott, T.R., Dance, S.L., 2010. Remote sensing of intertidal morphological change in Morecambe Bay, UK, between 1991 and 2007. Estuar. Coast. Shelf Sci. 87, 487–496. https://doi.org/10.1016/j.ecss.2010.01.015.
Miles, J.W., Lee, Y.K., 1975. Helmholtz resonance of harbours. J. Fluid Mech. 67, 445–464.
Mullarney, J.C., Hay, A.E., Bowen, A.J., 2008. Resonant modulation of the flow in a tidal channel. J. Geophys. Res. Oceans 113, C10007. https://doi.org/10.1029/2007JC004522.
Murray, N.J., Clemens, R.S., Phinn, S.R., Possingham, H.P., Fuller, R.A., 2014. Tracking the rapid loss of tidal wetlands in the Yellow Sea. Front. Ecol. Environ. 12, 267–272.
Murray, N.J., Phinn, S.R., Clemens, R.S., Roelfsema, C.M., Fuller, R.A., 2012. Continental scale mapping of tidal flats across East Asia using the Landsat archive. Remote Sens. 4, 3417–3426. https://doi.org/10.3390/rs4113417.
Murray, N.J., Phinn, S.R., DeWitt, M., Ferrari, R., Johnston, R., Lyons, M.B., Clinton, N., Thau, D., Fuller, R.A., 2019. The global distribution and trajectory of tidal flats. Nature 565 (7738), 222–225. https://doi.org/10.1038/s41586-018-0805-8.
Pacheco, A., Ferreira, ó., Williams, J.J., 2011. Long-term morphological impacts of the opening of a new inlet on a multiple inlet system. Earth Surf. Processes Landforms, 36(13), 1726–1735.
Prandle, D., Rahman, M., 1980. Tidal response in estuaries. J. Phys. Oceanogr. 10, 1552–1573.
Ren, M.E., Zhang, R.S., 1985. On tidal inlets of China. Acta Oceanolog. Sin. 3, 423–432.
Ryu, J.H., Kim, C.H., Lee, Y.K., Won, J.S., Chun, S.S., Lee, S., 2008. Detecting the inter-tidal morphologic change using satellite data. Estuar. Coast. Shelf Sci. 78, 623–632. https://doi.org/10.1016/j.ecss.2008.01.020.
Sagar, S., Roberts, D., Bala, B., Lymburner, L., 2017. Extracting the intertidal extent and topography of the Australian coastline from a 28 year time series of Landsat observations. Remote Sens. Environ. 195, 153–169.
Sammartino, S., Sánchez Garrido, J.C., Delgado, J., Aldeanueva, C.N., Criado, F., García, L.J., 2014. Experimental and numerical characterization of harbor oscillations in the port of Málaga, Spain. Ocean Eng. 88, 110–119. https://doi.org/10.1016/j.oceaneng.2014.06.011.
Sener, E., Davraz, A., Sener, S., 2010. Investigation of Aksehir and Eber Lakes (SW Turkey) coastline change with multitemporal satellite images. Water Resour. Manag. 24 (4), 727–745. https://doi.org/10.1007/s11269-009-9467-5.
Siegle, E., Huntley, D.A., Davidson, M.A., 2004. Physical controls on the dynamics of inlet sandbar systems. Ocean Dyn. 54 (3–4), 360–373.
Sridhar, R.S., Elangovan, K., Suresh, P.K., 2009. Long term shoreline oscillation and changes of Cauvery delta coastline inferred from satellite imageries. J. Indian Soc. Rem. Sens. 37 (1), 79–88. https://doi.org/10.1007/s12524-009-0013-y.
Stiller, D., Ottinger, M., Leinenkugel, P., 2019. Spatio-temporal patterns of coastal aquaculture derived from Sentinel-1 time series data and the full Landsat archive. Remote Sens. 11 (14), 1707.
Stumpf, R.P., Holderied, K., Sinclair, M., 2003. Determination of water depth with high-resolution satellite imagery over variable bottom types. Limnol. Oceanography, 48 (1,Part 2), 547–556.
Sun, C., Fagherazzi, S., Liu, Y., 2018. Classification mapping of salt marsh vegetation by flexible monthly NDVI time-series using Landsat imagery. Estuarine, Coastal Shelf Sci. 213, 61–80.
Sutherland, G., Garrett, C., Foreman, M., 2005. Tidal resonance in Juan de Fuca Strait and the Strait of Georgia. J. Phys. Oceanography 35 (7), 1279–1286.
Wang, D., Wang, Y.P., Yang, Y., Gao, J.H., Yang, Y., 2016. The characteristics and mechanism of suspended sediment transport in lagoon: a case study from Xincun and Li-an harbors, Hainan island. Quaternary Sci. 26 (1), 154–162.
Wang, Y.X., Liu, Y.X., Jin, S., Sun, C., Wei, X.L., 2019. Evolution of the topography of tidal flats and sandbanks along the Jiangsu coast from 1973 to 2016 observed from satellites. J. Photogram. Remote Sens. 150, 27–43. https://doi.org/10.1016/j. isprsjprs.2019.02.001.
Wang, X.X., Xiao, X.M., Zou, Z.H., Chen, B.Q., Ma, J., Dong, J.W., Doughty, R.B., Zhong, Q.Y., Qin, Y.W., Dai, S.Q., Li, X.P., Zhao, B., Li, B., 2018. Tracking annual changes of coastal tidal flats in China during 1986–2016 through analyses of Landsat images with Google Earth Engine. Remote Sens. Environ. https://doi.org/10.1016/j.rse.2018.11.030.
Wang, X.Z., Zhang, H.G., Fu, B., Shi, A.Q., 2013. Analysis on the coastline change and erosion-accretion evolution of the Pearl River Estuary, China, based on remote-sensing images and nautical charts. J. Appl. Rem. Sens. 7 (1), 073519. https://doi.org/10.1117/1.JRS. 7.073519.
Woodcock, C.E., Allen, R., Anderson, M., Belward, A., Bindschadler, R., Cohen, W., Gao, F., Goward, S.N., Helder, D., Helmer, E., 2008. Free access to Landsat imagery. Science 320. https://doi.org/10.1126/science.320.5879.1011a. 1011-1011.
Yang, D.T., Yang, C.Y., 2009. Detection of seagrass distribution changes from 1991 to 2006 in Xincun Bay, Hainan, with satellite remote sensing. Sensors 9 (2), 830–844.
Yang, Y., Gao, S., Zhou, L., Wang, Y.W., Li, G.C., Wang, Y.P., Jia, P.H., 2016a. Grain size distribution of surface sediments and sedimentary environment in the lagoon of Xincun, Hainan Island. Acta Oceanol. Sin. 38 (1), 94–105.
Yang, Y., Gao, S., Zhou, L., Han, Z.C., Zhu, D., Wang, Y.W., Zhao, Y.Y., Wang, Y.P., Jia, P.H., 2016b. Analysis of tides and P-A relationships of Xincun and Li-an lagoons, Southeastern Hainan island. Quatern. Sci. 26 (1), 163–172.
Zhang, Q.M., 1987. On P-A relationships of tidal inlets along South China coast. J. Trop. Oceanography 6 (2), 10–18.
Zhang, Q.M., Chen, X.S., Wang, W.J., Song, C.J., 1995. Geomorphological evolution of the entrances of the sandbar-lagoon type tidal inlets along the southern China coastlines. Acta Oceanolog. Sin. 17 (2), 69–77.
Zhao, B., Guo, H., Yan, Y., Wang, Q., Li, B., 2008. A simple waterline approach for tidelands using multi-temporal satellite images: a case study in the Yangtze Delta. Estuar. Coast. Shelf Sci. 77, 134–142. https://doi.org/10.1016/j.ecss.2007.09.022.